Applied Energy 203 (2017) 474–495

Contents lists available at ScienceDirect

Applied Energy

journal homepage: www.elsevier.com/locate/apenergy

1D + 3D two-phase flow numerical model of a proton exchange membrane fuel cell

Rui B. Ferreira, D.S. Falcão, V.B. Oliveira, A.M.F.R. Pinto *

Transport Phenomena Research Center (CEFT), Chemical Engineering Department, Faculty of Engineering of University of Porto, Rua Dr. Roberto Frias, 4200-465 Porto, Portugal

HIGHLIGHTS

- A 1D + 3D model of a PEM fuel cell is described and experimentally validated.
- VOF method tracks the two-phase flow and electrochemical reactions are considered.
- Water dynamics inside a serpentine channel is analyzed for different voltages.
- Water content in different regions of channel is quantified.
- Important issues on coupling of the VOF model with electrochemical reactions are addressed.

GRAPHICAL ABSTRACT

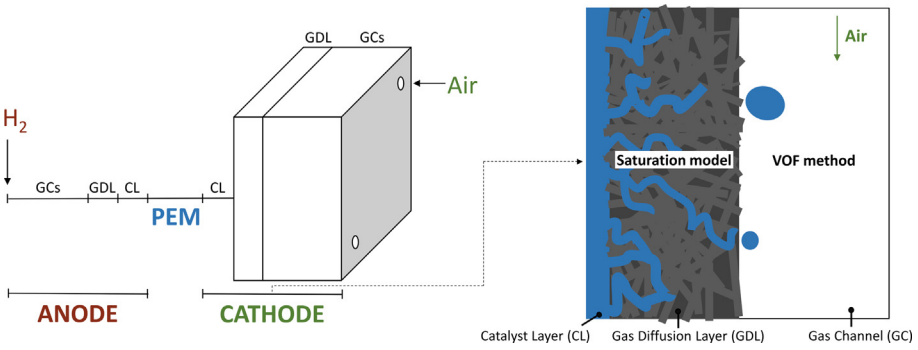

ARTICLE INFO

Article history:
Received 28 March 2017
Received in revised form 13 June 2017
Accepted 15 June 2017
Available online 23 June 2017

Keywords:
PEM fuel cells
Water management
Two-phase flow
Numerical model
Volume of fluid method

ABSTRACT

In this work, a numerical model of a proton exchange membrane (PEM) fuel cell is presented. The volume of fluid (VOF) method is employed to simulate the air-water two-phase flow in the cathode gas channel, at the same time that the cell electrochemical performance is predicted. The model is validated against an experimental polarization curve and through the visualization of water distribution inside a transparent fuel cell. The water dynamics inside a serpentine gas channel is numerically analyzed under different operating voltages. Moreover, water content in different regions of the channel is quantified. Current density and water generation rate spatial distributions are also displayed and it is shown how they affect the process of water emergence into the gas channel. Important issues on the simulation of the PEM fuel cells two-phase flow are addressed, especially concerning the coupling of the VOF technique with electrochemical reactions. Both the model and the numerical results aim to contribute to a better understanding of the two-phase flow phenomenon that occurs in these devices.

1. Introduction

In a proton exchange membrane (PEM) fuel cell, hydrogen and oxygen are electrochemically combined to generate electrical energy. High efficiency and power density, rapid and cold start-up, as well as low to zero emissions are characteristics that render these devices a viable power generation technology for the future. PEM fuel cells are specially promising as a sustainable alternative to the internal combustion motors for transportation.

Water management is one of the technical issues that impedes the widespread commercialization of PEM fuel cells. Although the membrane needs to be properly hydrated to guarantee high proton conductivity, the low temperature of a PEM fuel cell makes the appearance of liquid water inevitable. Water flooding can thus occur creating a gas-liquid two-phase flow that increases mass transport resistance and lowers the cell performance. Flooding also affects the cell durability. It accelerates platinum

* Corresponding author.
E-mail address: apinto@fe.up.pt (A.M.F.R. Pinto).

http://dx.doi.org/10.1016/j.apenergy.2017.06.048
0306-2619/

Nomenclature

a	water activity
A	area (cm^2)
C	molar concentration (mol m^{-3})
C^{ref}	reference molar concentration (mol m^{-3})
D	effective diffusion coefficient (m^2 s^{-1})
D^0	binary diffusion coefficient (m^2 s^{-1})
D_{cap}	capillary diffusion coefficient (kg m^{-3} s^{-1})
f	volume fraction
F	Faraday's constant (C mol^{-1})
$\vec{F}$	momentum source term (N m^{-3})
g	gravitational acceleration (N m^{-3})
I	current density (A cm^{-2})
I^{ref}	reference current density (A cm^{-2})
I_0^{ref}	reference exchange current density (A cm^{-2})
J	Leverett J-function
K	permeability (m^2)
M	molecular weight (kg mol^{-1})
n	total number of computational cells (Eq. (35)); surface normal (Eqs. (9), (10) and (26))
n_{drag}^{sat}	electro-osmotic drag coefficient in a fully hydrated membrane
$\hat{n}$	unit normal
N	molar flux (mol m^{-2})
OCV	open circuit voltage (V)
P	pressure (Pa)
P_{cap}	capillary pressure (Pa)
P_{sat}	saturation pressure (Pa)
Q	volumetric gas flow rate (m^3 s^{-1})
R	ideal gas constant (J mol^{-1} K^{-1})
r	resistance (Ω m^2)
RH	relative humidity
s	liquid water saturation
t	time (s)
$\hat{t}$	surface tangent
T	temperature (°C)
v	velocity (m s^{-1})
V	operating voltage (V)
w	water
x	Cartesian coordinate (direction of the 1D domain)
X	multiplicative factor for liquid water velocity
Y	mass fraction
Y^*	mass fraction at the cell adjacent to a wall

Greek symbols

α	membrane water transport coefficient
α_c	cathode transfer coefficient
δ	thickness (m)
ε	porosity
η	overpotential (V)
θ	contact angle (°)
κ	curvature of the interface (m^{-1})
λ	reactant stoichiometry (Eq. (19)); membrane water content (Eqs. (42)–(45))
μ	dynamic viscosity (Pa s)
ρ	density (kg m^{-3})
σ	proton conductivity (S m^{-1})
τ	surface tension (N m)

Superscripts

CL	catalyst layer
GC	gas channel
GDL	gas diffusion layer
m	exponent for effective porosity
n	exponent for effective saturation
PEM	proton exchange membrane
ref	reference value
sat	saturation value

Subscripts

a	anode
c	cathode
cap	capillary
i	specie (Eqs. (13), (14), (26)); counter for the number of computational cells (Eq. (35))
PEM	proton exchange membrane
sat	saturation value
w	liquid water

dissolution-precipitation and carbon support corrosion that degrades the catalyst layers (CLs) [1]. Moreover, it also speeds-up the corrosion of the gas diffusion layers (GDLs) and the membrane, which in turn raises the ohmic losses [1]. Another negative effect of flooding is the increase of pressure drop that can reduce the overall system efficiency.

In the last two decades, experimental studies related with the two-phase flow in PEM fuel cells were published with several techniques being employed, including optical visualization [2–9], magnetic resonance imaging [10,11], neutron imaging [12–15] and X-ray radiography [16–18]. Experimental tests have been extremely valuable, giving important information on the main two-phase flow patterns and their relation with cell performance for different operating conditions and material properties. However, visualization techniques often require materials and/or cell designs that are significantly different from those applied in industrial PEM fuel cells, which makes current experimental work not able of precisely reproduce the actual behavior of an operating cell. Moreover, it is challenging to extract relevant quantitative results from such experiments. This leads investigators to perform mathematical modeling and simulation in order to obtain more quantitative insights into the two-phase flow and its consequences. In this respect, the volume of fluid (VOF) method has become popular owing to its ability to consider surface tension and wall adhesion effects and the capacity to track the interface between fluids.

The present authors published a review [19] related with simulations of the two-phase flow in PEM fuel cells where VOF model was employed, discussing the focus and numerical details of each study as well as the main outcomes. One of the issues of using the VOF method was found to couple this model with the electrochemical reactions taking place in a PEM fuel cell, because of the different length and time scales between the different phenomena. In a recent review on multiphase flow modeling [20], the great discrepancies in the time and length scales of the physical processes occurring in a PEM fuel cell are also emphasized, and simulation and modeling methods (and the corresponding computational cost) that can be applied at given scale are presented. Due to such difficulties, the great majority of the numerical studies on the two-phase flow in PEM fuel cells employing the VOF method has focused on water flow mainly from a fluid dynamics perspective, analyzing its emergence, accumulation and movement, and how it is affected by operating conditions, material properties and cell design. There are, however, a few attempts considering electrochemical reactions along with VOF method, including the works

from Le and Zhou [21–24], Chen et al. [25] and Ding et al. [26–28]. Le and Zhou [21] presented a very complete model of a PEM fuel cell. This three-dimensional (3D) model is unsteady and multiphase considering the VOF technique. It couples energy, momentum and species transport with charges transport for all the main components of a PEM fuel cell: membrane; CLs; GDLs; gas channels (GCs); and current collectors (CCs). The model was employed to study the effects of liquid water on the velocity field, pressure, reactants and temperature distributions as well as on current density for cells with single-serpentine [21], multi-serpentine [23] and interdigitated flow fields [22]. It was also employed to a three-cell PEM fuel cell stack [24]. Despite the complexity and the important outcomes provided by this model, one important disadvantage is that calculations were performed by manually placing water droplets on the cathode GCs, instead of water being continuously emerging from the GDL surface, as verified in a real fuel cell. In the work conducted by Chen et al. [25], water was already considered being emerging from the GDL surface. The authors used oxygen mass fraction at the bottom of the GDL to estimate the current density thought Tafel equation. Liquid water behavior in a straight GC was visualized, and its effects on mass transport and current density distribution were analyzed under different air inlet velocities and GC walls wettability. Ding et al. [26] considered a 3D domain for a straight cathode GC, and simplified the rest of the domain to 1D. Cathode overpotential was also obtained through Tafel expression. In addition, ohmic losses were also considered when predicting the cell performance. The model was used to investigate the effects of two-phase flow patterns on the PEM fuel cell performance for different gas flow rates and GDL surface wettabilities. The studies published by Chen et al. [25] and Ding et al. [26] provide some new insights on how to consider electrochemical reactions when applying the VOF technique, without the need for the complexity present in models such as that developed by Le and Zhou [21], which often limits their practicability due to the large computational times involved. However, some issues can still be addressed in order to obtain a more comprehensive model with a larger range of applicability. In relation to Chen et al. [25], the velocity of liquid water entering into the GCs is set manually to an arbitrary value, instead of being calculated as function of the current density produced. Moreover, water balance in the membrane is not considered. Ding et al. [26] added the feature of water velocity in each pore being related with water generation rate nearby. However, although ohmic losses are considered to better predict the current density, the membrane is considered fully humidified. In both studies, the model applicability is limited in the sense that they cannot predict the influence of strategies dealing with two-phase flow issues that might have negative effects on the hydration state of the membrane (*e.g.* increasing the gas flow rate or the cell temperature). Another aspect that is missing in the studies where electrochemical reactions are considered along with the VOF methodology is the validation of the cell performance predicted by the models against experimental polarization curves.

The objective of this work is to move one step forward on PEM fuel cell modeling and simulation, more specifically on coupling the VOF method to simulate the two-phase flow with the electrochemical reactions taking place in the cell, addressing some of the limitations related with the above mentioned studies. A numerical model is presented that simulates the air-water flow in the cathode, together with the current being produced in the CLs and also the water balance in the membrane. Moreover, a hybrid 1D + 3D computational domain is implemented that allows to capture the relevant physical details of a complete fuel cell with reasonable simulation times. The model is first described in detail, then its predictions are quantitatively validated against an experimental I-V curve (polarization curve) and qualitatively by visualizing liquid water distribution inside a transparent PEM fuel cell. Finally, results from the model simulations are shown and discussed, with the aim of gathering a better understanding on the PEM fuel cells two-phase flow and its implications.

2. Model

2.1. Computational domain

In a PEM fuel cell, the most important performance losses are mainly related with the cathode operation. One reason is the slower kinetics of the oxygen reduction reaction (ORR) in the cathode in comparison with that of the hydrogen oxidation reaction (HOR) occurring in the anode. The cathode is also the electrode where water is generated and, therefore, where flooding is generally more significant. Moreover, the flow rate, viscosity and density of air in the cathode are considerably higher than those of hydrogen in the anode, which also makes this electrode the most influential for the hydration state of the membrane. For these reasons, the model here proposed considers a 3D computational domain for the cathode GDL and GCs, being the cathode CL, the membrane and the anode side simplified to a 1D computational domain, as schematized in Fig. 1. This computational domain, inspired in previous works [26,29], allows to considerably decrease the grid requirements and to achieve acceptable computational times, without missing relevant physical details that influence the performance of a PEM fuel cell.

2.2. Strategy for simulating liquid water dynamics in the cathode

As mentioned in the Introduction, experimental and numerical research has provided important information on the two-phase flow in PEM fuel cells. Collecting information from such studies, water dynamics inside the cathode can be briefly described as follows: liquid water, mostly formed in the CL, moves through the GDL by capillary transport; it then emerges into the GCs in preferential sites of the GDL surface (generally those with cross-sections featuring the greatest spacing and thus with less capillary pressure resistance [30]) and forms water droplets; these droplets grow until they eventually detach from the GDL; after detachment, they can move downstream as single-droplets or they can coalesce with other droplets forming films and/or slugs. With constant water production rate (*i.e.*, constant current operation), this process tends to repeat itself. A scheme provided in Fig. 2 illustrates liquid water transport processes in the cathode side as well as its cyclic nature. It should also be noted that, due to local temperature and water

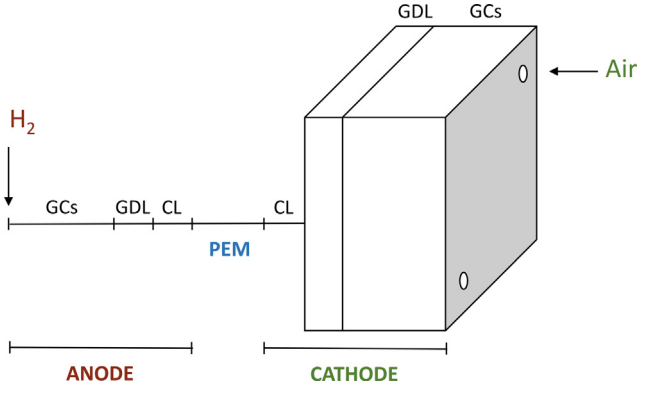

Fig. 1. Schematic representation of the computational domain employed in the present model.

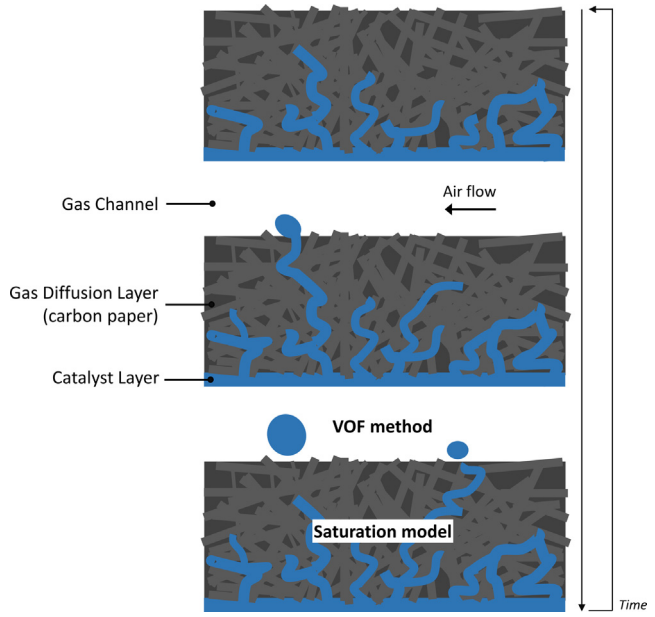

Fig. 2. Scheme of water dynamics in the cathode of a PEM fuel cell, and indication of the domains where the VOF method and saturation model are employed for simulating liquid water transport.

vapor concentration variations, liquid water may also be added into the cell by condensation, or removed by evaporation.

The numerical simulation of all these processes is a significant challenge. Early two-phase flow modeling approaches, the multiphase-mixture [31–34] and multi-fluid model [35–37], use a saturation model, where liquid water transport is assumed to be driven by capillary pressure, described by Darcy's law. This technique allows to reasonably describe the liquid flow inside the highly-resistant porous media, when appropriate effective transport properties are considered. However, in the above mentioned models, liquid water velocity in the GCs is assumed to be equivalent to the gas velocity (*i.e.*, a fine mist), making them incapable of identifying the presence of liquid droplets, films or slugs that accumulate in GCs. In order to adequately describe liquid water flow in the GCs, interface tracking algorithms, particularly the VOF method, have been employed. Theoretically, the VOF technique can also be applied to the scales of the porous media of PEM fuel cells. However, the GDLs complex microstructure should be included in the domain, making the resulting mesh untreatable with the current computational capacity. Another option is to use the homogeneous porous media formulation to consider liquid water transport in the GDL. However, this would result in an uniform liquid water transport through the porous media and an emergence in the GCs without the formation of droplets [38]. As explained above, this differs to that observed in a real PEM fuel cell.

In an attempt to adequately describe liquid water transport in the cathode of a PEM fuel cell, the present model considers two different two-phase flow approaches. In the GDL, liquid water transport is simulated with the multi-fluid saturation model. This approach allows to obtain the distribution of water in the GDL as liquid water saturation, and to compute its effects on the cell performance. In the GCs, several pores are designed at the GDL surface to represent the preferential pathways for liquid water emergence, and the VOF interface tracking technique is used to capture the dynamics of liquid water. Water velocity in each pore is obtained based on the water generation rate nearby. This approach, combining advantages of these two modeling techniques, allows to simulate the main two-phase flow processes in the cathode in practical manner and to achieve a wide range of applicability. In the illustration of Fig. 2 is also indicated the domain where each two-phase flow model is applied.

2.3. General assumptions

The present model relies on the following main assumptions:

- Gases are considered as ideal;
- Flow is consider laminar and under isothermal conditions;
- All materials are assumed to be isotropic;
- Gravity effect is neglected.

Other more specific assumptions and simplifications are considered for decreasing mathematical efforts and achieving more numerical stability. For better comprehension, such simplifications are presented below along with the model mathematical description.

2.4. Mathematical formulation

2.4.1. 3D domain

2.4.1.1. VOF method for tracking the interface. The VOF technique models unmixable fluids by solving a unique group of momentum equations and tracks the volume fraction of each fluid, as well as their interface, all over the domain. In each control volume, the sum of the volume fraction of all phases is equal to one. In the case of the present work, the volume fractions of air (f_{air}) and liquid water (f_w) are related by:

$$f_{air} + f_w = 1 \tag{1}$$

Tracking the interface is achieved by solving the equation below in each computational cell:

$$\frac{\partial f_w}{\partial t} + \nabla \cdot (f_w \vec{v}_w) = 0 \tag{2}$$

where $\vec{v}$ is the velocity. The governing equations are the continuity and momentum equations that have the following form:

$$\frac{\partial \rho}{\partial t} + \nabla \cdot (\rho \vec{v}) = 0 \tag{3}$$

$$\frac{\partial}{\partial t}(\rho \vec{v}) + \nabla \cdot (\rho \vec{v}\,\vec{v}) = -\nabla P + \nabla \cdot [\mu(\nabla \vec{v} + \nabla \vec{v}^T)] + \vec{F} \tag{4}$$

where P corresponds to the operating pressure, and ρ and μ are the volume-averaged density and dynamic viscosity, respectively, calculated by:

$$\rho = f_{air}\rho_{air} + f_w\rho_w \tag{5}$$

$$\mu = f_{air}\mu_{air} + f_w\mu_w \tag{6}$$

In the GCs, $\vec{F}$ is the force related with surface tension, adopting the continuum surface force (CSF) model introduced by Brackbill et al. [39]:

$$\vec{F} = \tau \frac{\rho \kappa_w \nabla f_w}{\frac{(\rho_{air} + \rho_w)}{2}} \tag{7}$$

where τ refers to surface tension coefficient, and κ_w is the curvature defined in terms of divergence of unit normal, $\hat{n}$:

$$\kappa_w = \nabla \cdot \hat{n} \tag{8}$$

where

$$\hat{n} = \frac{n}{|n|} \tag{9}$$

and n corresponds to the surface normal, defined as the gradient of f_w:

$$n = \nabla f_w \tag{10}$$

For the porous GDL, the Darcy drag force term is added into the momentum source term, thus $\vec{F}$ is obtained by:

$$\vec{F} = \tau \frac{\rho k_w \nabla f_w}{\frac{(\rho_{air}+\rho_w)}{2}} - \frac{\mu}{K}\vec{v} \tag{11}$$

where K represents the intrinsic GDL permeability. An important procedure applied in the present model should be mentioned here. In PEM fuel cells, liquid water enters the GCs in the form of droplets which diameter grows to values considerably larger than that of the GDL pores. Therefore, the GDL acts as a wall when liquid water from the GCs touches its surface. Due to its roughness, and because the GDLs are usually treated with Polytetrafluoroethylene (PTFE) in order to facilitate water removal, such surface has a hydrophobic nature. For this reason, most VOF numerical studies focusing on the two-phase flow in the GCs specify the GDL surface as a hydrophobic wall. However, in this work, setting the cathode GDL/GCs interface as a hydrophobic wall would inhibit the air flow through the GDL. This issue is overcome by specifying a lower value of K for the liquid phase. For air, K is set to 10^{-12} m^2, a typical value for GDL materials used in PEM fuel cells [40–43]. For liquid water, a value of 10^{-15} m^2 is used. This prevents water accumulation in the GDL, allowing to simulate the hydrophobic nature of its surface. Preliminary simulations were conducted in which the results obtained employing the present approach were compared with those where the GDL surface was set as an actual hydrophobic wall, and good agreement was achieved. It should be noted that, in the GDL, where liquid water transport is accounted by the multi-fluid saturation model, the appropriate value for liquid water permeability is employed, as it is shown in Table 3.

Wall adhesion is considered by using the contact angle that the fluid makes with the wall to adapt the surface normal in the cells near the wall. Considering θ as the contact angle at the wall, the surface normal ($\hat{n}$) at the cell close to the wall can be given by:

$$\hat{n} = \hat{n}_{wall}\cos\theta + \hat{t}_{wall}\sin\theta \tag{12}$$

where $\hat{n}_{wall}$ and $\hat{t}_{wall}$ correspond to the unit vectors normal and tangential to the wall, respectively.

2.4.1.2. Species transport. Since the gas-phase, air, is composed of several species, the conservation equation for each specie needs to be solved. It is given by:

$$\frac{\partial}{\partial t}(\varepsilon\rho_{air}Y_i) + \nabla\cdot(\rho_{air}Y_i\vec{v}) = -\nabla\cdot(\rho_{air}D_i\nabla Y_i) \tag{13}$$

where ε stands for porosity, and Y_i and D_i are the mass fraction and the effective diffusivity of specie i (O_2, H_2O or N_2), respectively. D_i is calculated by:

$$D_i = D_i^0 \varepsilon^m (1-s)^n \tag{14}$$

where s is the liquid water saturation. D_i^0 is the binary diffusion coefficient obtained using Fuller, Schettler and Giddings correlation [44]. In Eq. (14), Bruggeman correlation with exponents m and n equal to 1.5 has been largely applied [45–47]. However, it has been indicated that employing such values considerably overestimates D_i [46,47]. Here, m and n are both set equal to 3.5, taking into account recent measurements of the effective oxygen diffusivity in GDL materials commonly applied in PEM fuel cells [46].

Within the gas-phase and inside the GDL, the conservation equation for liquid water saturation (multi-fluid saturation model) is also solved, and it has the following form:

$$\frac{\partial}{\partial t}(\varepsilon\rho_w s) + \nabla\cdot[D_{cap}\nabla s] = 0 \tag{15}$$

where D_{cap} corresponds to the capillary diffusion coefficient, given by:

$$D_{cap} = \rho_w \frac{Ks^3}{\mu_w}\frac{dP_{cap}}{ds} \tag{16}$$

and P_{cap} is the capillary pressure, related with s by the Leverett J-function, defined as:

$$P_{cap}(s) = \frac{\tau\cos(\theta^{GDL})}{(K/\varepsilon)^{1/2}}J(s) \tag{17}$$

with $J(s)$ described by:

$$J(s) = \begin{cases} 1.417(1-s) - 2.120(1-s)^2 + 1.263(1-s)^3, & for\ \theta < 90^\circ \\ 1.417s - 2.120s^2 + 1.263s^3, & for\ \theta > 90^\circ \end{cases} \tag{18}$$

Leverett J-function was derived based on experimental data of homogeneous soil or a sand bed with constant wettability [48,49]. However, in the GDLs of PEM fuel cells, the size of the pores is not uniform, and their wettability is affected by both the hydrophilic carbon substrate and the hydrophobic agent. It has thus been reported that the Leverett J-function is not accurate enough to describe precisely liquid water saturation in the GDLs [50–52]. Although in several studies [43,53–56] experimental $P_{cap}(s)$ data for various GDL usually applied in PEM fuel cells have been obtained, there is no universal correlation similar to Leverett J-function for all GDL materials. Therefore, Leverett J-function is still applied in the present model, as it has been shown that it is capable of effectively describe qualitatively the effects of water flooding in the PEM fuel cell operation [50].

2.4.1.3. Boundary conditions. At the cathode air inlet, the velocity, v, and species mass fractions are specified as:

$$v = \frac{\lambda_{air}}{0.21}\frac{I^{ref}A_{active}}{4F}\frac{RT}{P}\frac{1}{A_{GC_c inlet}} \tag{19}$$

$$Y_{H_2O} = \frac{RH_{air}P_{sat}}{P} \tag{20}$$

$$Y_{O_2} = 0.21(1 - Y_{H_2O}) \tag{21}$$

$$Y_{N_2} = 0.79(1 - Y_{H_2O}) \tag{22}$$

where λ_{air} stands for the air stoichiometry, A_{active} is the cell active area, $A_{GC_c inlet}$ is the cross-section area of the cathode GC inlet, and RH_{air} corresponds to the relative humidity (RH) of air. In the present model, v is calculated for a fixed reference current density, I^{ref}, of 1.0 A cm^{-2}. Moreover, it is also specified that no liquid water enters in the cathode GC inlet by:

$$f_w = 0 \tag{23}$$

$$s = 0 \tag{24}$$

At the cathode GC outlet, pressure outlet boundary condition is used and gauge pressure is set.

At the solid walls, non-slip and zero diffusive flux for velocity and species boundary conditions, respectively, are prescribed:

$$v = 0 \tag{25}$$

$$\frac{\partial Y_i}{\partial n} = 0 \tag{26}$$

The only exception is the GDL bottom wall, where oxygen and water vapor mass fractions and liquid water saturation are specified, given by:

$$Y_{O_2} = Y^*_{O_2} + \frac{M_{O_2} N_{O_2} \Delta x}{D_{O_2} \rho_{air}} \tag{27}$$

$$Y_{H_2O} = Y^*_{H_2O} + \frac{M_{H_2O} N_{H_2O}(v) \Delta x}{D_{H_2O} \rho_{air}} \tag{28}$$

$$s = s^* + \frac{M_{H_2O} N_{H_2O}(l) \Delta x}{D_{cap}} \tag{29}$$

where Y^* and s^* refer to the corresponding values in the cells adjacent to the wall, and Δx is the distance between those cells center and the corresponding face at the wall. M corresponds to molecular weight. N_{O_2} is the oxygen molar flux, given by:

$$N_{O_2} = -\frac{I}{4F} \tag{30}$$

where I is the current density and F is the Faraday's constant. The values of water vapor molar flux, $N_{H_2O}(v)$, and liquid water molar flux, $N_{H_2O}(l)$, are obtained first considering the total water molar flux, N_{H_2O}, given by:

$$N_{H_2O} = (1 + \alpha)\frac{I}{2F} \tag{31}$$

where α corresponds to the membrane water transport coefficient, and comparing it with the corresponding value that would saturate the gas-phase with water vapor, $N^{sat}_{H_2O}$:

$$N^{sat}_{H_2O} = \frac{\left(Y^{Sat}_{H_2O} - Y^*_{H_2O}\right) D_{H_2O} \rho_{air}}{M_{H_2O} \Delta x} \tag{32}$$

where $Y^{Sat}_{H_2O}$ is the saturation mass fraction obtained based of saturation pressure. $N_{H_2O}(v)$ and $N_{H_2O}(l)$ are then calculated by:

$$\left.\begin{array}{l} N_{H_2O}(v) = N_{H_2O} \\ N_{H_2O}(l) = 0 \end{array}\right\} \; if \; N_{H_2O} \leqslant N^{sat}_{H_2O} \tag{33}$$

$$\left.\begin{array}{l} N_{H_2O}(v) = N^{sat}_{H_2O} \\ N_{H_2O}(l) = N_{H_2O} - N^{sat}_{H_2O} \end{array}\right\} \; if \; N_{H_2O} > N^{sat}_{H_2O} \tag{34}$$

Such computation considers that, after being produced in the CL, water first saturates the gas-phase, and the remaining amount condenses instantaneously into liquid water. This approximation eliminates the need to add source terms for water condensation/evaporation in the GDL, simplifying the model and increasing its numerical stability. Preliminary simulations were conducted using such source terms and the results obtained were close to those of the present approach. It is in the GDL bottom wall boundary condition that the 1D domain is incorporated into the 3D domain, providing the values of I and α needed in Eqs. (30) and (31). How such values are computed in the 1D domain is explained further ahead along this section.

At the pores placed in the bottom wall of the GCs (the GDL surface), corresponding to the liquid water inlets, the velocity in each pore is obtained by considering the liquid water produced in the area closest to it. First, the GDL is divided into the same number of areas as the number of pores, then the velocity of water in each pore is calculated by:

$$v = \frac{\frac{M_{H_2O}}{\rho_w} \sum_{i=1}^{i=n} N_{H_2O(l)_i} A_i}{A_{pore}} X \tag{35}$$

where i is the cell number and n is the total number of computational cells in the area closest to the pore. A_i corresponds to the area of the computational cell i, A_{pore} to the cross-section area of the pore and X is a multiplicative factor for liquid water velocity. Since water generation rate is very slow under the typical working conditions of a PEM fuel cell, theoretical values need to be amplified a few orders of magnitude to shorten the time for water accumulation in the GCs. Such modification does not alter significantly the nature of the flow due to the large flow ratio between air and liquid water, and is a current practice in PEM fuel cell numerical simulation when applying the VOF method [38,57,58]. In the present study, X is set to 400, a value within the range applied in the mentioned studies. In this boundary condition, it is also specified that only liquid water enters through the pores by setting:

$$f_w = 1 \tag{36}$$

2.4.2. 1D domain

As mentioned above, it is in the 1D domain that the current density, I, being produced by the cell at a specified voltage is computed. Tafel equation is employed for this purpose, described by:

$$I = (1 - s) I_0^{ref} \frac{C^{CL_c}_{O_2}}{C^{ref}_{O_2}} e^{\left(\frac{\alpha_c \eta_c F}{RT}\right)} \tag{37}$$

where I_0^{ref} and $C^{ref}_{O_2}$ correspond to the reference values of exchange current density and oxygen molar concentration, respectively. $C^{CL_c}_{O_2}$ is the oxygen molar concentration in the middle of cathode CL, α_c is the cathode transfer coefficient, R is the ideal gases constant and T is the cell operating temperature. η_c corresponds to the cathode overpotential and is calculated by:

$$\eta_c = OCV - V - I r_{ohm} \tag{38}$$

where OCV refers to the open circuit voltage, V to the cell operating voltage and r_{ohm} to the ohmic resistance.

In Eq. (37), s is directly provided by the 3D domain (s^*). Here, the transport of liquid water in the CL water is neglected, as it would increase considerably the mathematical complexity. Since the CL is very thin, this would not significantly affect the model predictions. $C^{CL_c}_{O_2}$ can be obtained taking the oxygen molar concentration in the cathode GDL/CL interface, $C^{GDL_c/CL_c}_{O_2}$, and subtract the oxygen transfer resistance (based on Fick's law) in the CL:

$$C^{CL_c}_{O_2} = C^{GDL_c/CL_c}_{O_2} - \frac{I}{4F} \frac{\delta^{CL_c}/2}{D^{CL_c}_{O_2}} \tag{39}$$

where δ^{CL_c} refers to the cathode CL thickness. $C^{GDL_c/CL_c}_{O_2}$ is obtained by:

$$C^{GDL_c/CL_c}_{O_2} = \frac{Y^{GDL_c/CL_c}_{O_2} \rho_{air}}{M_{O_2}} \tag{40}$$

where $Y^{GDL_c/CL_c}_{O_2}$ corresponds to the value of $Y^*_{O_2}$, provided by the 3D domain.

Electrical bulk resistance is generally negligible. In well-designed fuel cells, electrical contact resistances are also minimal. Proton resistance in the CL is also usually much smaller than that in the membrane. Therefore, r_{ohm} in Eq. (38) is here approximated by the proton resistance in the membrane. This resistance is obtained by integrating the inverse of membrane proton conductivity, σ_{PEM}, over its thickness, δ^{PEM}. For simplicity, in present work r_{ohm} is approximated by:

$$r_{ohm} = \frac{\delta^{PEM}}{\sigma_{PEM}} \tag{41}$$

being σ_{PEM} given by [59]:

$$\sigma_{PEM} = 10^{-2}(0.005139\lambda - 0.00326)e^{[1268(\frac{1}{303}-\frac{1}{273+T})]} \quad (42)$$

where λ corresponds to the water content in the membrane. λ used in Eq. (42) is computed as the average between the anode and cathode values.

In order to obtain λ, one needs to account for the water balance in the membrane. In this study, the water molar flux in the membrane, $N_{H_2O}^{PEM}$, is computed by considering electro-osmotic drag and back diffusion [59]:

$$N_{H_2O}^{PEM} = \alpha\frac{I}{2F} = 2n_{drag}^{sat}\frac{I}{2F}\frac{\lambda}{22} - \frac{\rho_{PEM}}{M_{PEM}}D_{PEM}\frac{d\lambda}{dx} \quad (43)$$

where n_{drag}^{sat} corresponds to the electro-osmotic drag coefficient in a fully hydrated membrane, ρ_{PEM} to the dry membrane density, M_{PEM} to the membrane molecular weight, and x to direction of water transport in the membrane. D_{PEM} is the water diffusion coefficient in the membrane, obtained by [59]:

$$D_{PEM} = 10^{-10}(2.563 - 0.33\lambda + 0.0264\lambda - 0.000671\lambda^2)e^{[2416(\frac{1}{303}-\frac{1}{273+T})]} \quad (44)$$

λ is computed by:

$$\lambda = \begin{cases} 14a, & anode \\ 12.6 + 1.4a, & cathode \end{cases} \quad (45)$$

where a corresponds to the water activity given by:

$$a = \frac{C_{H_2O}^{CL/PEM}RT}{P_{sat}} \quad (46)$$

and P_{sat} is the saturation pressure, obtained by (adapted from [59]):

$$P_{sat} = 100000 \times 10^{-2.1794+0.02953T-9.1387\times10^{-5}T^2+1.4454\times10^{-7}T^3}, T\ in\ ^\circ C \quad (47)$$

Both expressions for λ in Eq. (45) are based in measurements conducted by Springer et al. [59]. However, in order to simplify the calculations, the anode expression used in this work is a linear approximation [60] of the original correlation. Eq. (45) also implies that a is between 0 and 1 in the anode, and between 1 and 3 in the cathode, which is often the case in PEM fuel cells operation.

The water vapor molar concentrations in both sides of the membrane, needed to obtain the corresponding values of a, are calculated by:

$$C_{H_2O(v)}^{CL_a/PEM} = C_{H_2O(v)}^{A_{GC_a inlet}} - \alpha\frac{I}{2F}\left(\frac{\delta^{GDL_a}}{D_{H_2O}^{GDL_a}} + \frac{\delta^{GDL_a}}{D_{H_2O}^{GDL_a}} + \frac{A^{GC_a/GDL_a}}{Q_{H_2}}\right) \quad (48)$$

$$C_{H_2O(v)}^{CL_c/PEM} = C_{H_2O(v)}^{GDL_c/CL_c} + (1+\alpha)\frac{I}{2F}\frac{\delta^{CL_c}}{D_{H_2O}^{CL_c}} \quad (49)$$

where $C_{H_2O(v)}^{A_{GC_a inlet}}$ refers to the water vapor molar concentration in anode GCs inlet, A^{GC_a/GDL_a} to the total area of the anode GCs facing the GDL, and Q_{H_2} to the anode volumetric gas flow rate. Eq. (48) considers the mass transfer resistance of water vapor in the porous CL and GDL, and the anode GCs are considered as a continuously stirred tank reactor (CSTR). Eq. (49) is analogue to Eq. (39) and $C_{H_2O(v)}^{GDL_c/CL_c}$ is obtained using $Y_{H_2O}^{GDL_c/CL_c}$ (corresponding to $Y_{H_2O}^*$) provided by the 3D domain.

2.5. Numerical implementation

The present model is implemented in the computational fluid dynamics (CFD) commercial code ANSYS Fluent, version 15.0. The 1D domain is incorporated into the 3D domain through User Defined Functions (UDFs) written in C programming language. At each iteration, $Y_{O_2}^*$, $Y_{H_2O}^*$, and s^* in every computational cell adjacent to the GDL bottom wall are provided by the 3D computation. These values, together with the anode operating conditions and kinetic and cell design parameters, are used in the 1D domain to calculate I and α. These values are then used to adjust the GDL bottom wall species boundary condition in the 3D domain.

In the 1D domain calculations, D_{PEM} is considered constant when integrating Eq. (43), so an analytical solution can be obtained. Such simplification lies in the fact that D_{PEM} does not vary considerably in the range of $4 < \lambda < 20$, and in PEM fuel cells operation λ is usually between those values. After substituting Eqs. (44)–(49) in Eq. (43) (after integration), and performing some algebraic manipulations, α can be explicitly obtained as function of I. The α expression is then inserted into Eqs. (48) and (49) and, using Eqs. (45)–(47), σ_{PEM} (Eq. (42)) can also be obtained as function of I. Placing the expression of σ_{PEM} in Eq. (41) and then Eqs. (38)–(41) in Eq. (37) results into an analytic equation having I as the unique unknown. This equation is then numerically solved using the Newton–Raphson method. After convergence, the calculated values of I and α are used in Eqs. (30) and (31) to obtain the new values of Y_{O_2}, Y_{H_2O}, and s to be returned to the 3D domain.

Regarding the 3D domain solution methods, pressure-based segregated solver is adopted for the incompressible flow, and the explicit VOF formulation is applied to track the interface between fluids. The gaseous species equations in the gas-phase are solved using the built-in species transport model. For liquid water saturation, the conservation equation for a User Defined Scalar (UDS) within the gas-phase is solved, being the flux and unsteady functions as well as the diffusion term defined through UDFs. SIMPLE scheme is used for pressure-velocity coupling. Least squares cell based method is adopted for gradient spatial discretization, whereas PRESTO! scheme is employed for pressure discretization. Momentum discretization is achieved through the second order upwind methodology. The geometric reconstruction scheme is used to represent the interface between fluids using the piecewise-linear interface calculation (PLIC) from the work of Youngs [61]. First order upwind scheme is employed for spatial discretization of gaseous species and liquid water saturation equations. The varying time-step method is used applying a maximum global courant number of 2.

2.6. Calculation procedure

The first step of the calculation procedure is to obtain a steady-state solution. In this initial stage, the VOF method is not activated (by setting the liquid water velocity in each pore equal to 0). The results of this solution comprise species (including water saturation in the GDL), current density, pressure and velocity distributions. The results of this steady-state solution are then used as the initial values for the two-phase flow transient calculation. Because in the beginning of the transient calculation, the liquid water generation ($N_{H_2O}(l)$) is already available in all the domain, the water velocity can be obtained for all the pores designed at the GDL surface (Eq. (35)). Such procedure decreases considerably the overall simulation time. It is also in accordance with the real operation of a PEM fuel cell, because the distribution of gaseous species along the cell occurs much more rapidly than the liquid water distribution.

2.7. Computational geometry and mesh

The mesh used in the simulations consists on an unstructured mesh with 1,259,416 tetrahedral elements with minimum and maximum size of 7.0×10^{-5} m and 2.5×10^{-4} m, respectively, for a 25 cm^2 PEM fuel cell with a single-serpentine flow field. ANSYS

Table 1
Features of the meshes employed to investigate the effect of the mesh size.

Mesh	Min. size (m)	Max. size (m)	Elements number (type)	Nodes number
1	7.0×10^{-5}	2.5×10^{-4}	36,237 (tetrahedral)	7582
2	5.0×10^{-5}	2.0×10^{-4}	101,652 (tetrahedral)	20,170
3	2.0×10^{-5}	7.0×10^{-5}	355,374 (tetrahedral)	68,543
4	4.0×10^{-5}		342,941 (hexahedral)	1,452,514

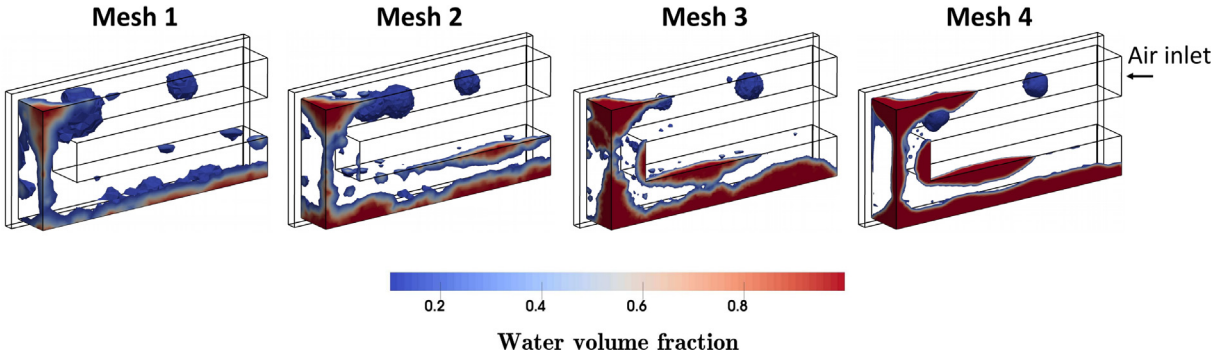

Fig. 3. Water distribution (at about 30 ms) in a U-shaped channel with different meshes.

Table 2
Time-averaged (from 0 to 30 ms) volume-weighted water content (percentage of the channel volume that is occupied by water) in a U-shaped channel with different meshes.

Mesh	Volume-weighted water content in the U-shaped channel
1	3.67%
2	4.64%
3	5.05%
4	4.99%

Meshing was used for mesh generation. The mesh size was selected after performing a mesh size test. A small computational domain considering a 14.2 mm long U-shaped channel having two pores at the GDL surface was used in such analysis in order to employ more refined meshes. Apart from meshes having tetrahedral elements, a very refined mesh with hexahedral elements was also tested. Table 1 shows the main features of the meshes considered. Fig. 3 depicts the water distribution in the U-channel and Table 2 displays the volume-weighted water content. It can be seen that the results of Mesh 3 are in good agreement with those from Mesh 4, both qualitatively (Fig. 3) and quantitatively (Table 2). Mesh 1 and Mesh 2 present more significant differences (especially Mesh 1) regarding the amount of water in the channel (Table 2). However, when analyzing water distribution in the channel (Fig. 3), the results are reasonable. It can be seen that both coarser meshes can capture the general two-phase flow pattern, which is water accumulation and movement along the upper corners of the channel. Moreover, the shape of the water droplets emerging from the GDL surface is very similar for all meshes tested. In this study, a computational domain for a 25 cm^2 fuel cell had to be employed because the experimental results used to validate the model were obtained testing cells with such size (see Section 3). Implementing such a large computational domain considerably limits the mesh density that can be applied. For this reason, Mesh 1 was used in the simulations conducted in this work. Even applying this coarse mesh, the simulation time for a single case (*i.e.*, a single voltage) exceeded two months, in a computer having a Intel Core i7-2600 K @ 3.40 GHz CPU (all 8 processes used) and 8 GB RAM.

For water emergence into the GCs, two pores with a diameter of 200 μm are designed at the GDL surface of each channel, equally distant from the side walls. Such profile of water transport from the GDL to the GCs is just a simplification of that occurring in a real PEM fuel cell. The preferential pathways for water transport through the GDL are not fixed and may change over time [62], and the number of pathways may also change according with the operating conditions (*e.g.*, water would emergence into the GCs from more places (pores) when the current density is higher, because more water is being produced in such condition). Nevertheless, together with the procedure for calculating water velocity in each pore (see Section 2.4.1.3), it gives a reasonably account of the process of water emergence into the GCs. The diameter employed for each pore was chosen in order to represent the largest pores found in the GDL, from which liquid water tends to move. This is a value within the range employed in other VOF numerical studies [26,63] and has the same order of magnitude of the largest pores of GDLs, as reported in studies addressing the structural features of such materials [64,65]. Fig. 4 displays the geometry (Fig. 4A), indicating the air inlet and the pores designed at the GDL (water inlets), and details of the mesh (Fig. 4B) of the computational domain applied in this work.

3. Experimental

3.1. I-V curve and kinetic parameters determination

The PEM fuel cell test station described in a recent study [66] from the present authors was used for the experimental tests. The same cell hardware (active area of 25 cm^2) as that employed in Ref. [66] was also applied. A commercial membrane electrode assembly (MEA) supplied by QuinTech e.K. was employed, containing 0.3 and 0.6 mg Pt cm^{-2} in the anode and cathode, respectively; Freudenberg carbon paper as GDLs (reference H23 I2); and Nafion 212 as the electrolyte. The contact angle of the GDL and GCs walls (machined into graphite surfaces) was measured to be 138.3 ± 9.1° and 89.3 ± 0.9°, respectively (OCA 15 plus optical contact angle system, DataPhysics Instruments). The values presented refer to the average between measurements made at three different locations on the respective surface followed by the standard deviation.

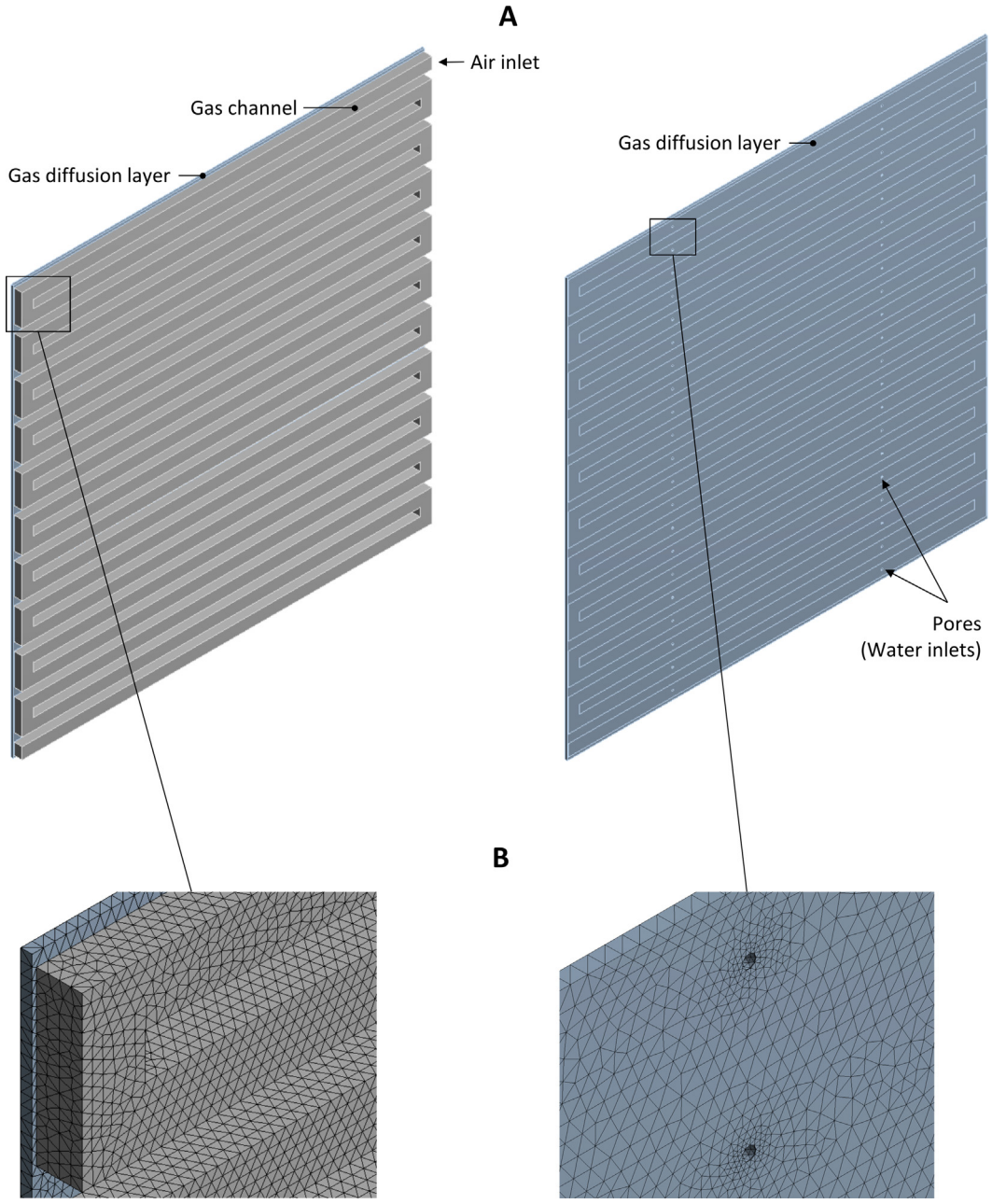

Fig. 4. Images of the computational (A) geometry and (B) mesh applied in the simulations of this work.

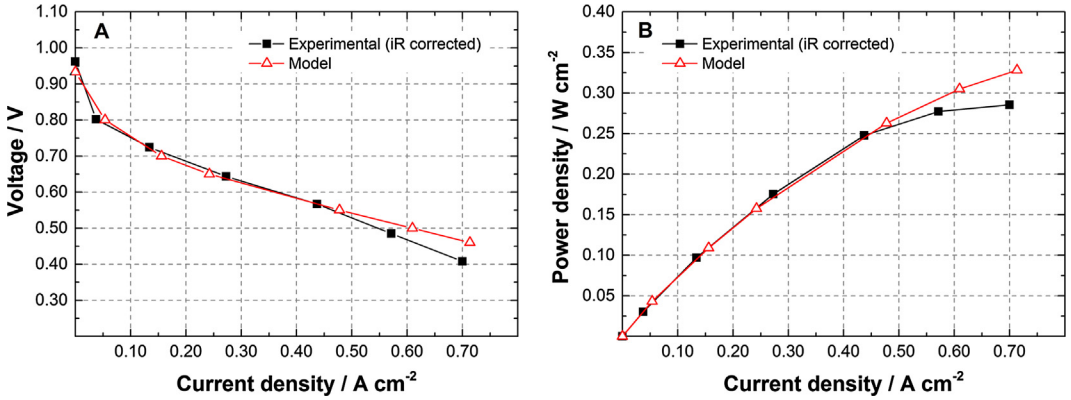

Fig. 5. Fuel cell performance obtained experimentally and calculated by the present model. A – Polarization curve; B – Power density curve.

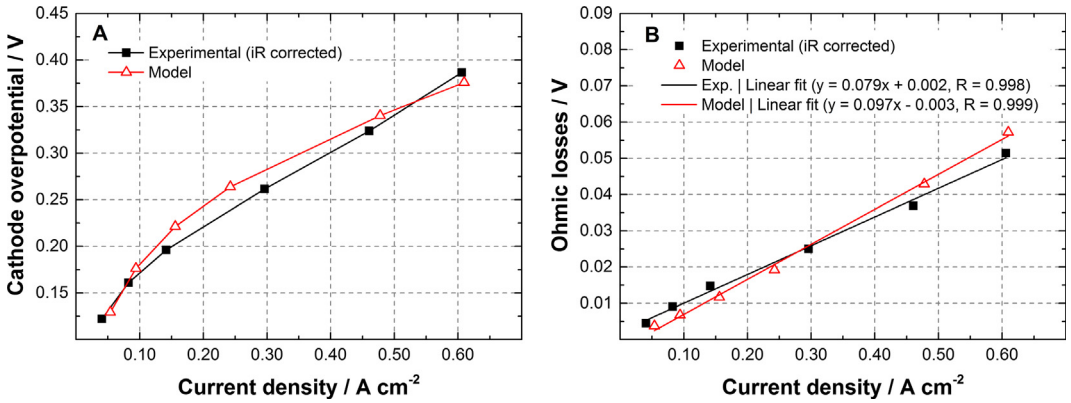

Fig. 6. Individual voltages losses obtained experimentally through EIS measurements and calculated by the present model. A – Cathode overpotential; B – Ohmic losses.

Table 3
Model input parameters.

Parameter	Value
Active area, A_{active}	25×10^{-4} m^2
GCs width	1.4×10^{-3} m
GCs height	1.0×10^{-3} m
Anode CL thickness, δ^{CL_a}	60×10^{-6} m (assumed)
Anode GDL thickness, δ^{GDL_a}	250×10^{-6} m[a]
Anode CL porosity, ε^{CL_a}	0.4 (assumed)
Anode GDL porosity, ε^{GDL_a}	0.5 (assumed)
Cathode CL thickness, δ^{CL_c}	60×10^{-6} m (assumed)
Cathode GDL thickness, δ^{GDL_c}	250×10^{-6} m[a]
Cathode CL porosity, ε^{CL_c}	0.4 (assumed)
Cathode GDL porosity, ε^{GDL_c}	0.5 (assumed)
GDL permeability for air, K_{air}	10^{-12} m^2 [40–43]
GDL permeability for liquid water, K_w (VOF method)	10^{-15} m^2 (assumed, see Section 2.4.1.1)
GDL permeability for liquid water saturation, K_w (saturation model)	2.55×10^{-13} m^2 [68]
Channel walls contact angle, θ^{GCs}	50.3° (measured, see Section 3.2)
GDL contact angle, θ^{GDL}	134.0° (measured, see Section 3.2)
Electro-osmotic drag coefficient, n_{drag}^{sat}	2.7 [59]
Membrane molecular weight, M_{PEM}	1.1 kg mol^{-1}
Membrane dry density, ρ_{PEM}	1970 kg m^{-3} [69]
Membrane thickness, δ^{PEM}	50.8×10^{-6} m [69]
Cathode transfer coefficient, α_c	0.343 (measured, see Section 3.1)
Reference exchange current density, I_0^{ref}	0.011 A cm^{-2} (measured, see Section 3.1)
Reference oxygen concentration, $C_{O_2}^{ref}$	7.641 mol m^{-3} (C_{O_2} at the cell inlet)
Open circuit voltage, OCV	0.933 V (measured, see Section 3.1)
Temperature, T	40 °C
Absolute pressure, P	1 atm
Hydrogen stoichiometry, λ_{H_2}	1.1
Air stoichiometry, λ_{air}	2.2
Relative humidity at the anode inlet, RH_{H_2}	50%
Relative humidity at the cathode inlet, RH_{air}	90%

[a] Internal thickness at 0.025 MPa. Information provided by the MEAs supplier.

Tests were conducted at 40 °C cell initial temperature (measured placing a thermocouple of type-K at the cathode outlet in contact with the MEA) and atmospheric pressure (considered to be 1 atm). In the anode, H_2 stoichiometry of 1.1 (for 1.0 A cm^{-2}) and RH of 50% (referenced for the cell initial temperature) were used. In the cathode, air stoichiometry was set to 2.2 and RH to 90%. Both gases were fed to the cell at 45 °C. Prior experiments, the MEA was conditioned. First, the voltage was set to 0.6 V for 30 min. Then, cycles of 0.7 V and 0.5 V (20 min at each voltage) were conducted, each one followed by a polarization curve. The conditioning procedure was finished when no improvement in the cell performance was observed.

I-V measurements were conducted in the potentiostatic mode, starting at the OCV and decreasing the voltage until 0.30 V, waiting 3 min at each voltage. I-V curves were repeated until performance stabilization was achieved, typically when the average difference between subsequent curves was less than 10%. Electrochemical impedance spectroscopy (EIS) was conducted right after polarization curves for determination of the kinetic parameters I_0^{ref} and α_c. Spectra were obtained at 0.80 V, 0.75 V, 0.70 V, 0.60 V, 0.50 V and 0.40 V by superimposing a 5 mV AC signal over a frequency range from 0.1 mHz to 100 kHz. A stabilization time of 3 min was also employed at each voltage. Impedance spectra were fitted to an electric equivalent circuit by the complex non-linear regression least squares fitting using the Thales Software from Zahner. The electric analogue used to fit the EIS spectra is shown and described in Ref. [66].

3.2. Visualization of liquid water inside a transparent PEM fuel cell

A ClearPak fuel cell from Pragma Industries, also with 25 cm^2 active area, was employed to visualize liquid water behavior inside the cathode GCs. Two 20.0 mm thick end-plates made of transparent polycarbonate allow the optical access to the GCs. A single-serpentine flow field, also having GCs with 1.0 mm height and 1.4 mm width, is engraved in both polycarbonate plates. A metallic mesh is employed between the GDLs and the end-plates to collect the current produced. The MEA used, also provided by Pragma Industries, has 0.3 and 0.6 mg Pt cm^{-2} in the anode and cathode, respectively; carbon paper as GDLs; and Nafion XL as the electrolyte. GDL and GCs (polycarbonate plates) surfaces contact angles were measured obtaining values of 134.0 ± 3.5° and 50.3 ± 0.2°, respectively. Before being assembled in the ClearPak, the MEA was conditioned employing the non-transparent fuel cell hardware and the procedure described above.

For the visualization experiments both gases were fed into the cell at 40 °C with RH of 50% and 90% for H_2 and air, respectively. H_2 and air stoichiometries were set to 1.1 and 2.2, respectively. Current density was set to 0.1 A cm^{-2} for 5 min and pictures of the cathode GCs were recorded each 2 s using a digital camera (Canon EOS 30D). Before measurements, the cell was left at the OCV for 20 min. The reason for operating the cell at low current is related with limitations of the materials employed in the transparent fuel cell. The polycarbonate endplates have very low thermal conductivity, so the heat produced by the cell was hardly removed. Therefore, the cell temperature tended to increase rapidly when higher currents were applied, evaporating all liquid

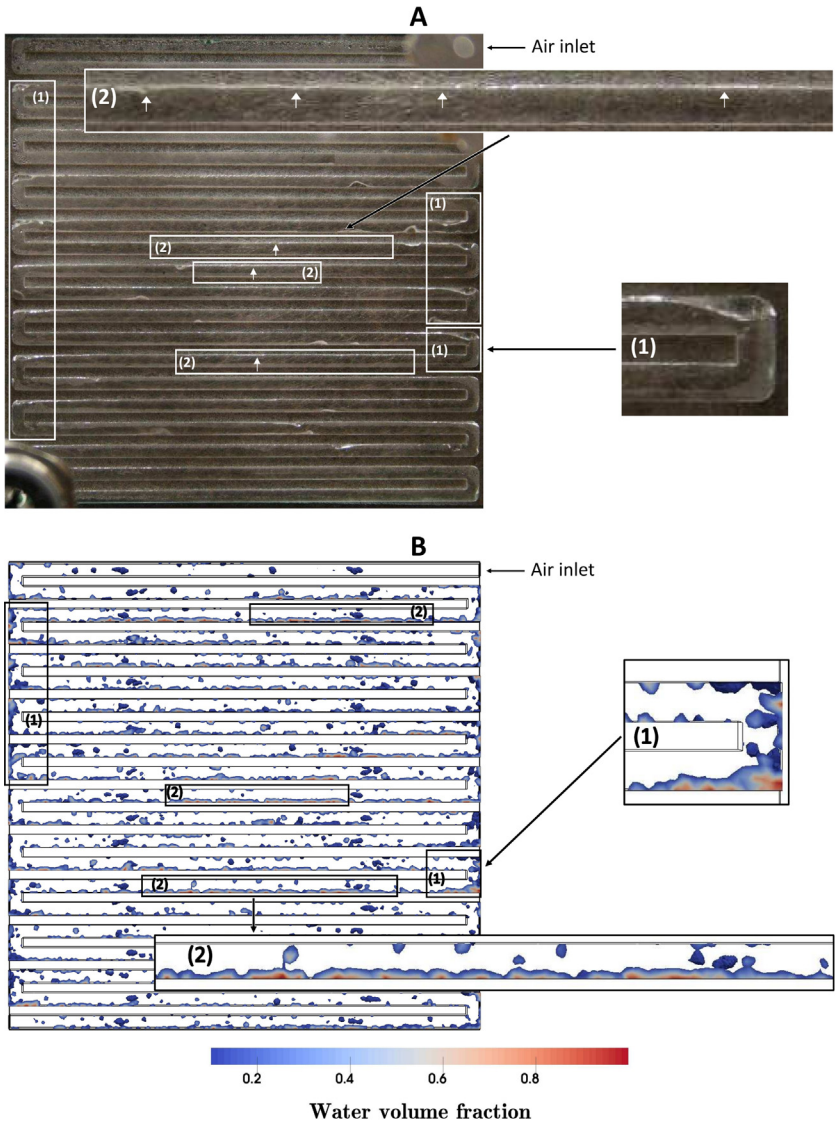

Fig. 7. Images of liquid water distribution inside the serpentine channel of a 25 cm^2 PEM fuel cell. A – Photographic of the cathode of an operating transparent PEM fuel cell; B – Simulation results from the present model. (1) Water accumulation at the elbows; (2) Water films attached to the walls of the channel.

water. Applying a current density of 0.1 A cm^{-2} allowed to keep the cell temperature below the reactants inlet temperature (40 °C), so liquid water remained in the cell and its distribution could be visualized.

4. Results and discussion

In the present section, results of the model are shown and discussed. First, its experimental validation is addressed. The model is validated in terms of its ability to predict the cell electrochemical performance and to simulate the two-phase flow in the cathode GCs. Water dynamics in the serpentine channel over time is then numerically analyzed, showing its emergence as droplets from the GDL pores, interaction with the walls and accumulation in the channel. Current density and liquid water generation rate spatial distributions are displayed, and their relation with the water velocity in each pore is demonstrated. Pressure drop, an important parameter for the efficiency PEM fuel cells systems that is strongly affected by the two-phase flow, is also analyzed for various operating voltages. An important advantage of conduct numerical simulations on the two-phase flow in PEM fuel cells is the possibility of extracting relevant quantitative data. Therefore, water content quantification is performed in different locations of channel. Finally, liquid water saturation in the GDL obtained by the multi-fluid saturation model is depicted and its effects on the cell performance are discussed.

4.1. Experimental validation

In Fig. 5 is depicted the cell performance in terms of polarization (Fig. 5A) and power density (Fig. 5B) curves simulated by the model here presented and that obtained experimentally. The experimental results are corrected taking into account the internal electrical resistance (iR) of the cell, which was found to be exceptionally high for the hardware employed, about 0.16 Ω cm^2, accounting for more than 2/3 of the cell total resistance. Such high value of iR was found to be caused by poor electrical contacts between the cell components, namely between the graphite plates and the GDLs. From the analysis of Fig. 5, a good agreement between the model predictions and the cell experimental performance can be observed. However, at high current densities, it

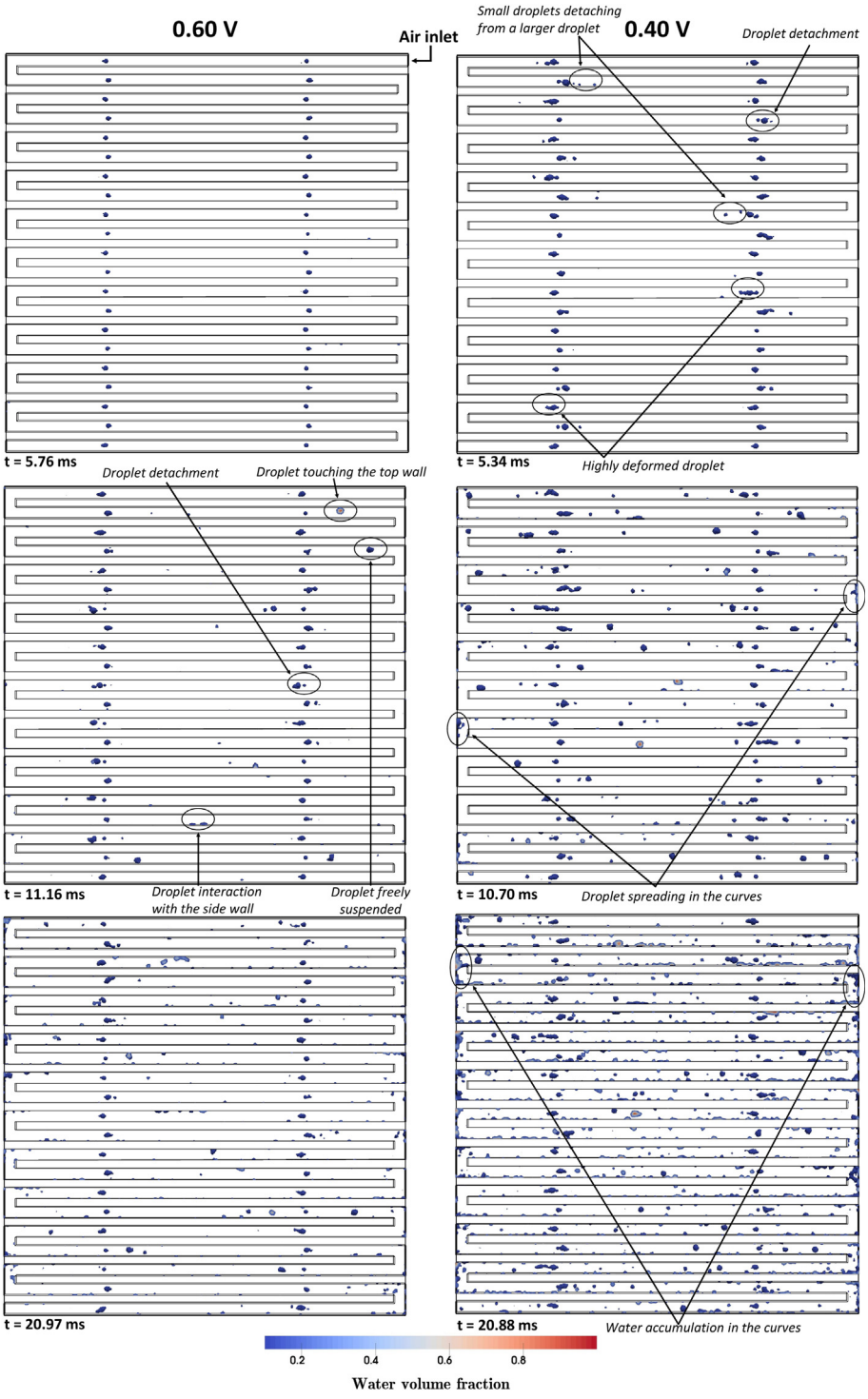

Fig. 8. Water dynamics in the serpentine channel for two different operating voltages.

can be seen that the model overpredicts the experimental results. At 0.70 A cm^{-2}, the simulated voltage is about 15% higher than that obtained experimentally. This is probably due to the usage of the Leverett J-function to calculate liquid water saturation, which may be inappropriate for the GDLs of PEM fuel cells, as already discussed in Section 2. The level of liquid water saturation might be underpredicted by this correlation, similarly to that reported by Ramos-Alvarado et al. [51], causing the model to overpredict the cell performance at high currents, where the effects of flooding are significant.

In Fig. 6 are displayed the individual voltage losses, including the cathode overpotential (Fig. 6A) and ohmic losses (Fig. 6B), obtained experimentally through impedance measurements and those calculated by the present model. It can be seen that the model is able to correctly separate the different contributions that affect the cell operation. The voltage decrease with increasing current density is mainly dominated by the cathode overpotential, which includes losses from the activation of the electrochemical reactions, and mass transfer resistance due to flooding occurring at high currents.

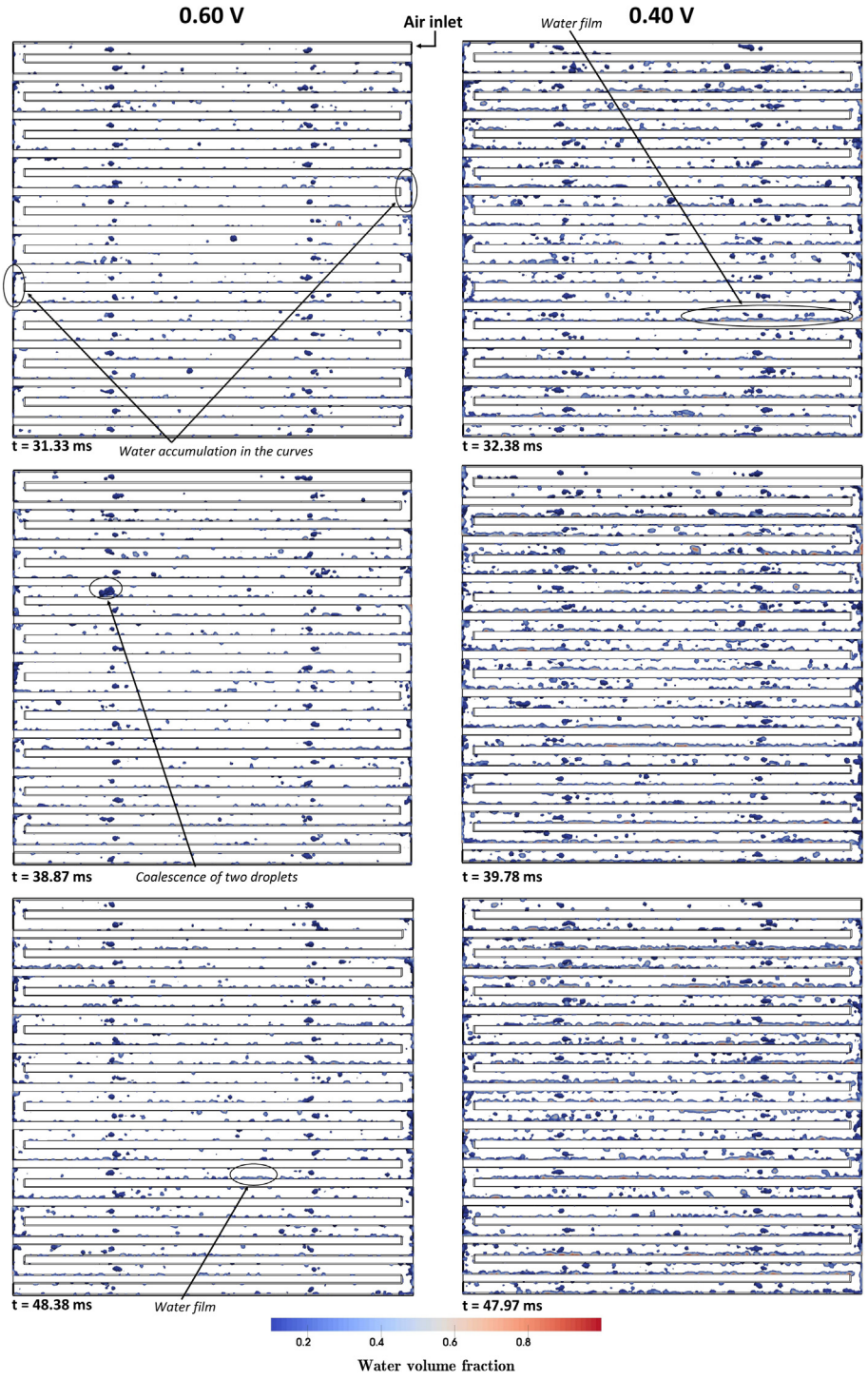

Fig. 8 (*continued*)

In Table 3 are shown the model input parameters giving rise to the results presented in this work. Parameters related with the fuel cell design and operating conditions were set equal to those employed in the experiments. Moreover, important kinetic parameters, namely the OCV, the cathode transfer coefficient, α_c, and reference exchange current density, I_0^{ref}, were obtained experimentally. This eliminates the need to arbitrarily assume such values, therefore increasing the accuracy of the model predictions. A recent study [67] stresses out the importance of gathering reliable and robust input data, with focus on the kinetics of the electrochemical reactions, in order to assure an adequate predictive capability of PEM fuel cells models.

Fig. 7 contains images of liquid water distribution inside the serpentine channel of an operating transparent fuel cell (Fig. 7A) and that simulated by the present model (Fig. 7B). The images shown were obtained after a relatively stable operation was achieved, in which the general flow patterns did not change considerably over time. The temporal analysis of the processes of water emergence, accumulation and movement before reaching such state are analyzed in the next section, using the model

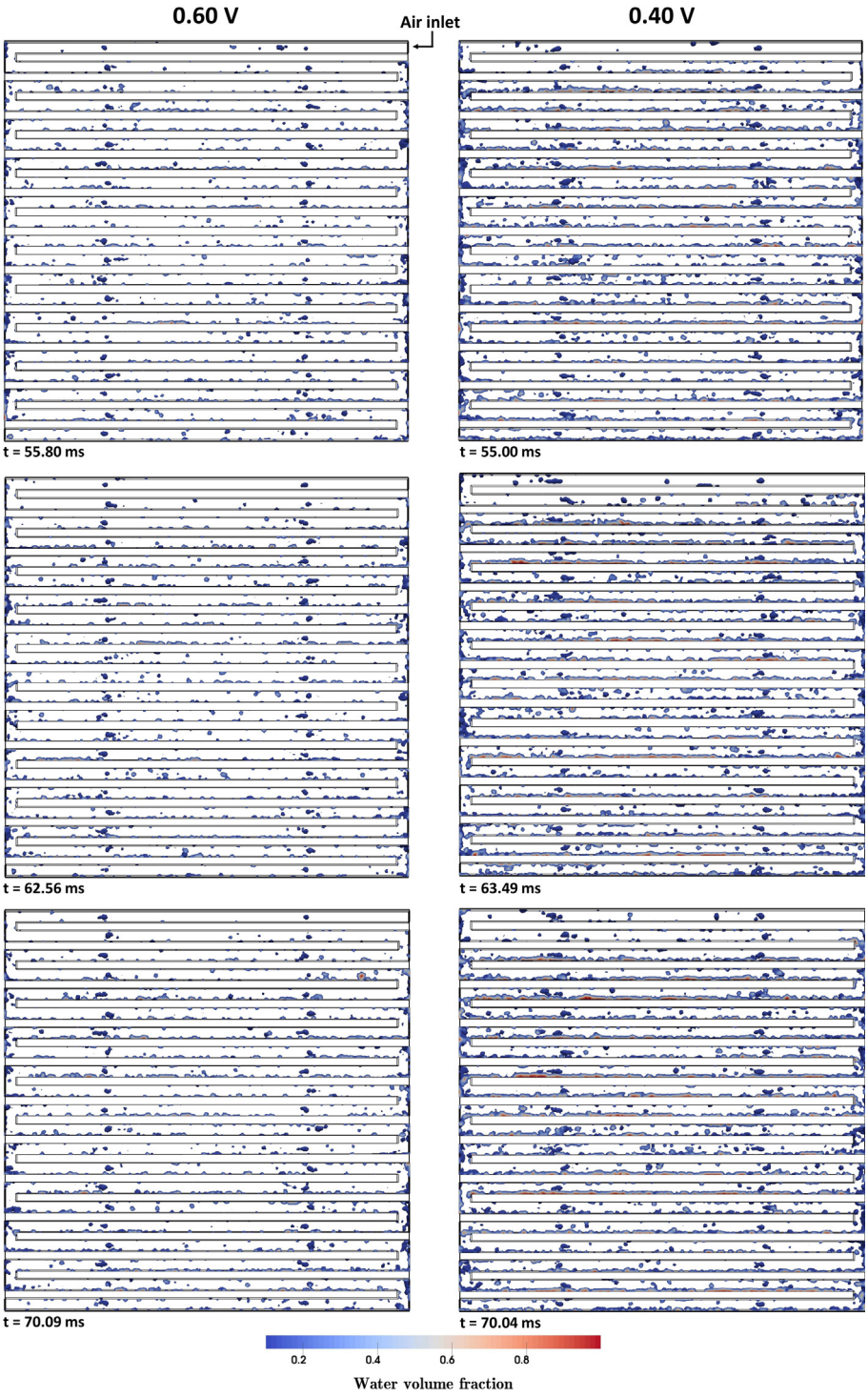

Fig. 8 (*continued*)

simulations. From the analysis of Fig. 7, it can be seen that the present model can capture the general liquid water flow patterns observed experimentally. In both situations, it can be observed a general trend for water to be accumulated in, or close to, the elbows of the channel (Fig. 7A(1) and B(1)). This occurs due to the low air velocity verified in the corners of these locations. Moreover, the formation of long water films attached to the (hydrophilic) walls of the channel can also be visualized in the experimental and simulation results (Fig. 7A (2) and B (2)). It is important to note that such comparison consists on a qualitative one. In the experiments, the exact location of water emergence is not controllable. Moreover, as already explained, water generation rate in the simulations has to be increased to achieve practical simulation times (see Section 2.4.1.3). Several *ex-situ* experiments [70–72] have been conducted, where the liquid water flow is visualized in micro-channels especially designed to simulate those of a PEM fuel cell, using a syringe pump to precisely control water emergence location and velocity. The conditions of such tests could be replicated in numerical simulations employing the VOF method, and the results (liquid water distribution [70–72], droplets departure

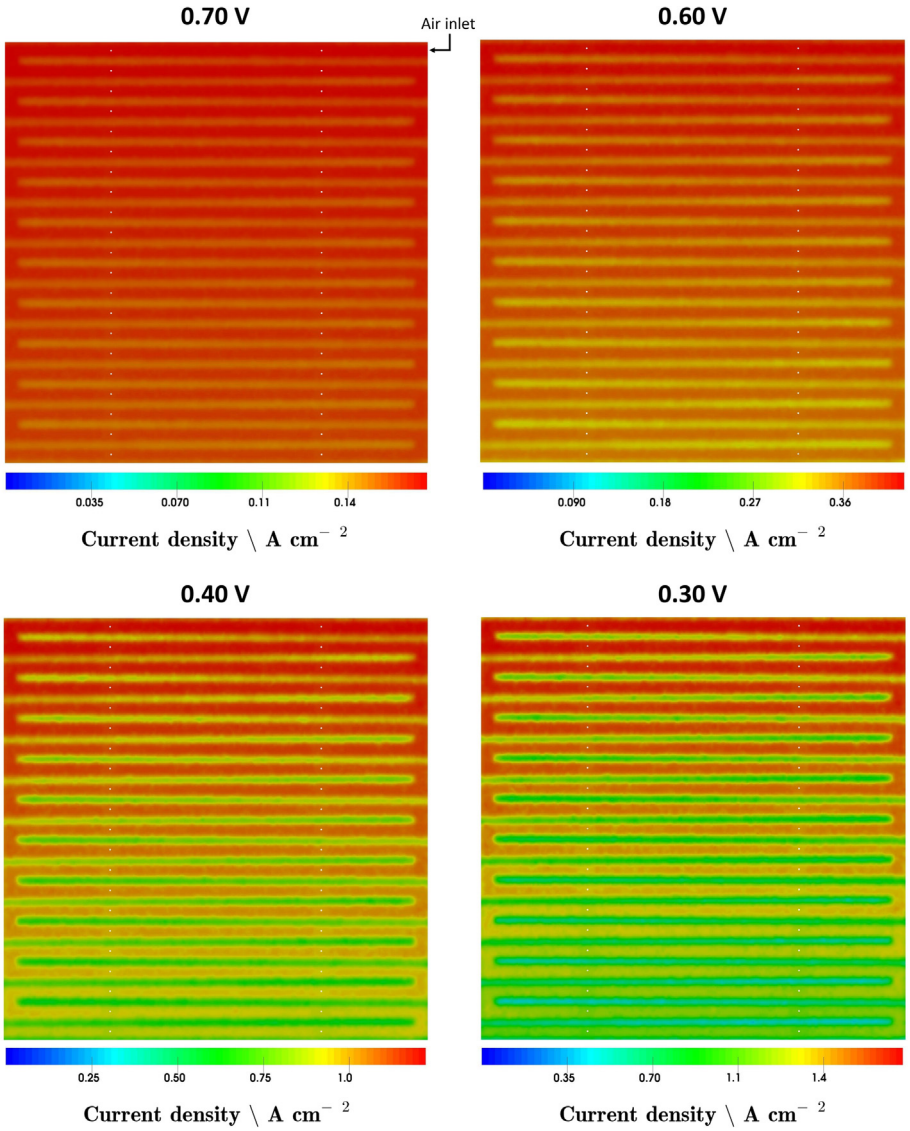

Fig. 9. Current density distribution for various operating voltages.

time [70] and two-phase flow pressure drop [72]) were almost identical to those obtained experimentally, clearly asserting the suitability of the VOF method to simulate the two-phase flow in conditions similar to PEM fuel cells.

4.2. Water dynamics inside the serpentine channel

Fig. 8 shows liquid water volume fraction in the serpentine channel at various time instants for two different operating voltages: 0.60 V and 0.40 V. Simulations for 0.70 V, 0.50 V and 0.30 V were also conducted. However, since the analysis of the results for 0.60 V and 0.40 V is sufficient to capture the effects of operating voltage in liquid water distribution, they are not shown here with the purpose of brevity.

For 0.60 V, at 5.76 ms, it can be seen liquid water emerging into the channel through the pores designed at the GDL surface, representing the main pathways for water transport, and the formation of droplets that grown in size with time. It can also be observed that these droplets do not suffer much deformation and are still attached to the GDL surface. For 0.40 V and at 5.34 ms, the droplets are generally larger, several are considerably deformed, and some already detached from the GDL surface, starting to move downstream. It can also be visualized some smaller droplets being ripped out from larger droplets due to the influence of the air flow. At 0.40 V, current density is higher (Figs. 5 and 9), more water is generated (Fig. 10), and thus water velocity in each pore is higher (Fig. 11). Results shown in Figs. 9–11 are discussed in detail in the next sub-section. Because more water is entering through each pore, droplets grow into a larger size and interact more significantly with the air flow, and considerable deformation occurs. At 0.60 V and 11.16 ms, several droplets already detached from the GDL surface and start to move along the channel. It can be observed some of these droplets moving freely suspended in the channel, and others interacting with the top and side walls of it. Moreover, as captured at 38.87 ms for 0.60 V, two droplets can interact with each other coalescing into a larger droplet. At 10.70 ms, for the case of 0.40 V, some of the droplets already reached and spread into the elbows of the serpentine channel. At 20.88 ms, for the same voltage, it can already be observed the tendency of water accumulation in the elbows of the channel and, at 32.38 ms, the first water films become visible. For the case at 0.60 V, water accumulation in the elbows of the channel only starts to be verified at 31.33 ms, and the first (small) water films are first visualized at 48.38 ms. From Fig. 8, it is also clear that, at any time,

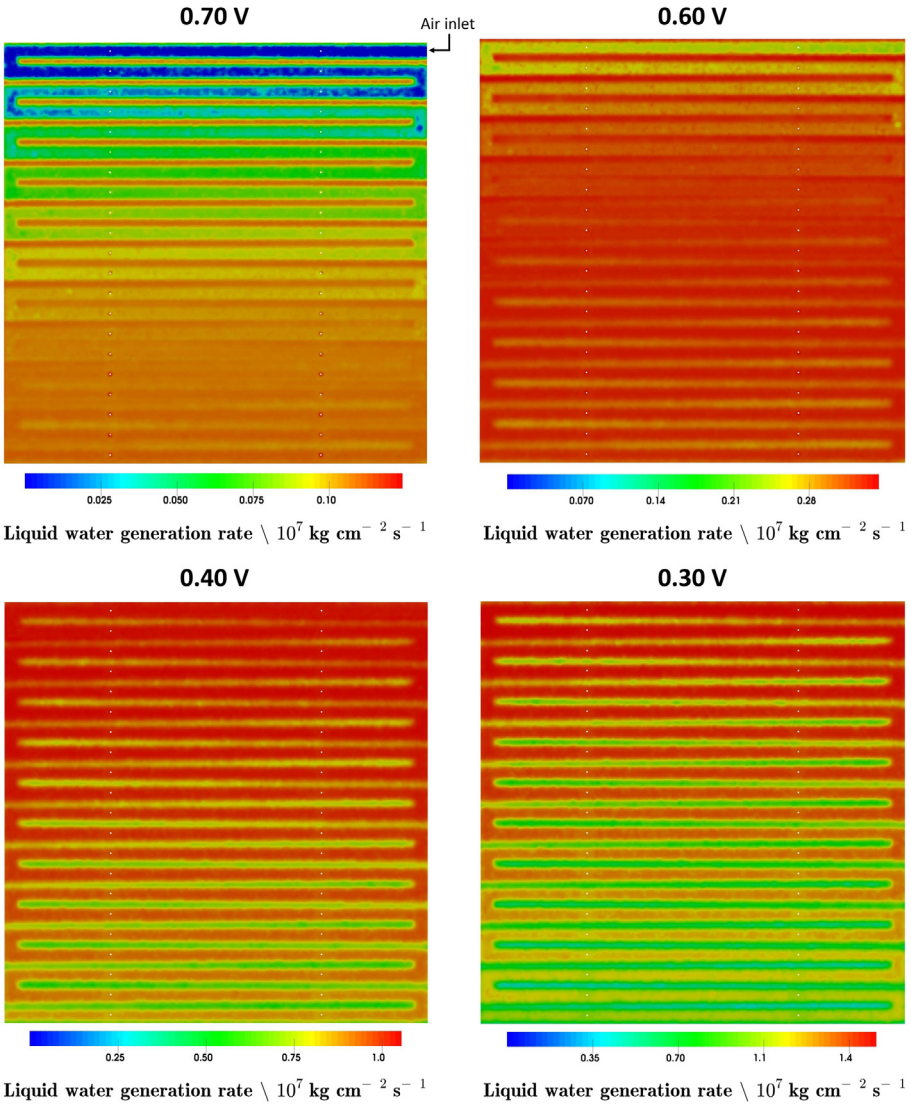

Fig. 10. Liquid water generation rate distribution for various operating voltages.

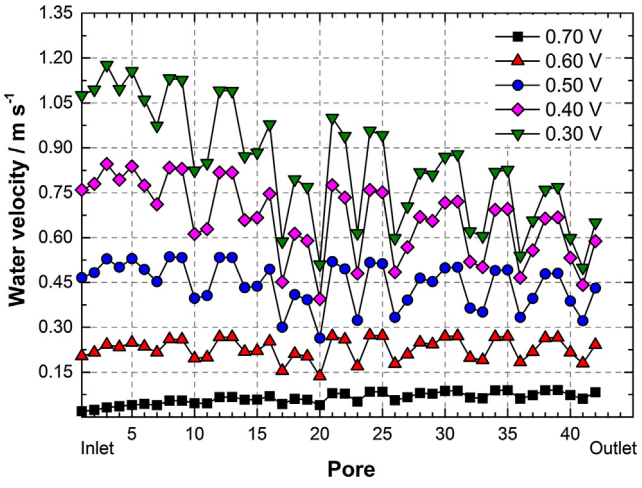

Fig. 11. Water velocity in each pore designed at the GDL surface.

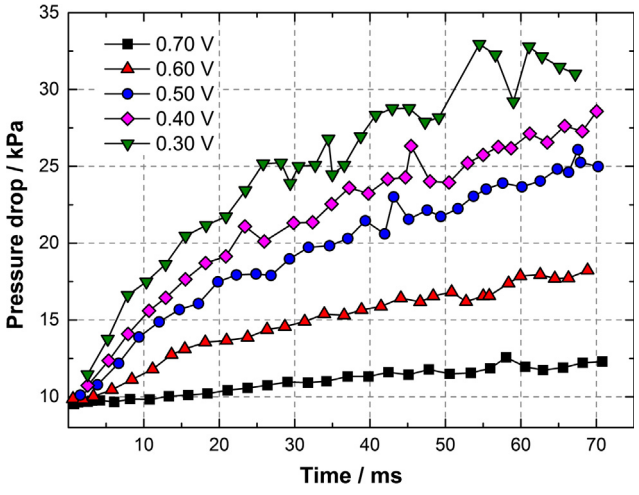

Fig. 12. Two-phase flow pressure drop at various operating voltages.

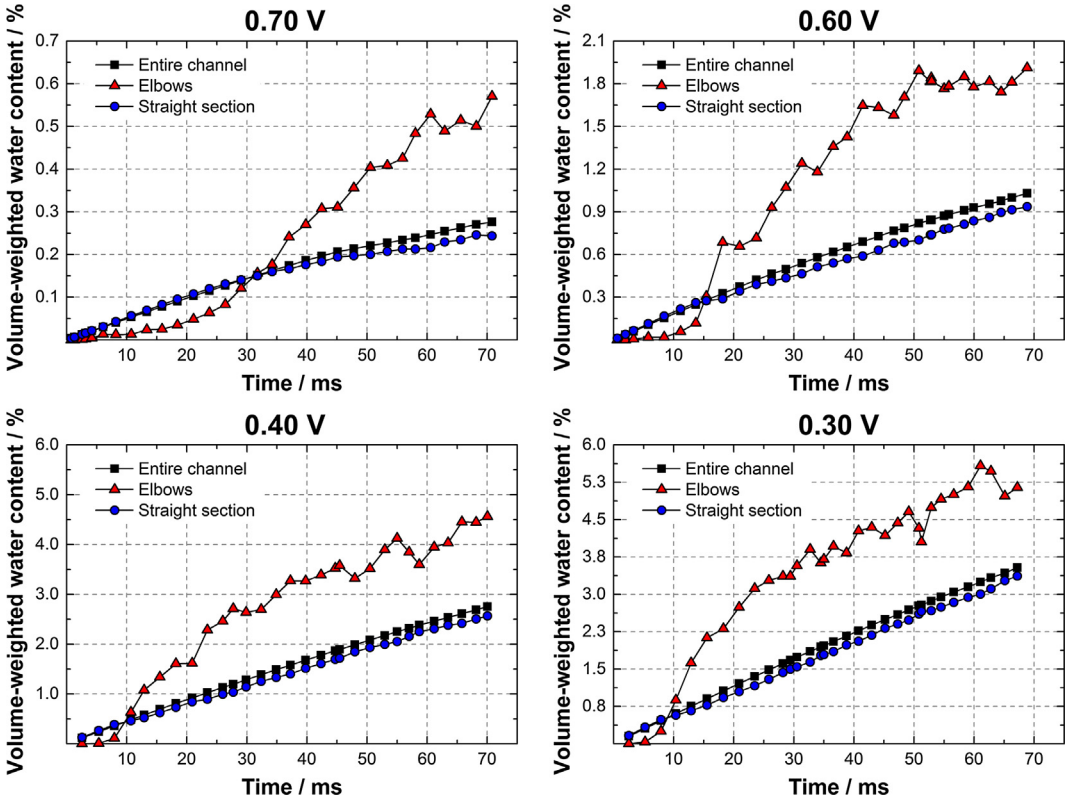

Fig. 13. Volume-weighted water content in the entire serpentine channel, in its straight sections and in its elbows, at various operating voltages.

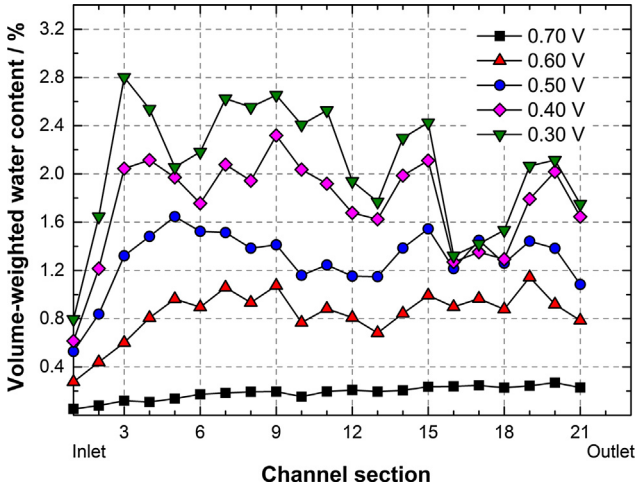

Fig. 14. Time-averaged volume-weighted water content in different sections of the serpentine channel at various operating voltages, after dividing the channel into 21 approximately equal sections, from the inlet to the outlet.

more water is present in the channel for the case of lower voltage. Moreover, after a certain time, liquid water flow patterns do not change considerably. This can be more easily observed for the case of 0.40 V, in which similar liquid water distribution patterns are observed from 32.38 to 70.04 ms. The most noted change during such interval is only on the amount of water present in the channel.

An important remark should here be made about the time scale of the results shown in this work. As mentioned in Section 2.4.1.3, the theoretical values of water velocity were increased in order to speed-up water accumulation in the channel and reduced the simulation time. That makes the characteristic time of the numerical results here presented to be the millisecond (ms). However, in real PEM fuel cells, the processes of water emergence and accumulation in the GCs has a higher characteristic time, from few seconds to minutes [2,5,8,73,74].

4.3. Current density and liquid water generation rate distributions and water velocity in each pore

Fig. 9 contains the current density spatial distribution for different operating voltages. The results obtained at 0.50 V are not shown in Fig. 9 for the sake of simplicity, as they agree with those from 0.40 V and 0.30 V. The same consideration is applied to Figs. 10 and 16. As expected, and as shown in Fig. 5, higher current densities are obtained for lower voltages. For all voltages, the current density is higher in the areas adjacent to serpentine channel, because in this region the convective flow of air is stronger and oxygen reaches the reactive sites more rapidly. It can also be observed that current density decreases along the channel length in all cases, from the inlet to the outlet, because oxygen is being consumed along the channel and its mass fraction decreases. Moreover, the decrease of current along the channel is more significant for lower voltages, because oxygen consumption rate is higher in such conditions.

Contrarily to current density, liquid water generation rate distribution along the cell active area varies when changing the operating voltage, as shown in Fig. 10. For 0.70 V, liquid water generation rate generally increases along the channel length, until it stabilizes close to the outlet. At such voltage, water production rate (directly proportional to current density) is low. In the area close to the inlet, the water vapor being produced is generally insufficient to saturate the air stream, and therefore liquid water generation rate is very low. However, as air continues to move along the channel, it continues to uptake water vapor, until it becomes saturated. This results into more significant amounts of

liquid water being generated. As shown in Fig. 9, current density does not decrease considerably along the channel, so does water production rate. Therefore, liquid water generation rate tends to stabilize at the region close to outlet. For 0.40 V and 0.30 V, water production rate is high, and the air stream becomes saturated right after entering the cell. In such cases, the current density, and thus water production rate, decreases significantly along the channel. Because all water produced condensates, liquid water generation rate also decreases along the channel. An intermediate case between those just described occurs at 0.60 V. Close to the channel inlet, liquid water generation rate is lower, and then increases in the middle region. However, because the decrease of current density and water production along the channel is higher than that verified at 0.70 V, liquid water generation rate tends to decrease in the region closer to the outlet. This is also the case with more uniform liquid water generation rate.

In Fig. 11 is depicted the water velocity in each pore for different operating voltages. Pore 1 is that closest to the air inlet and pore 42 is that closest to the outlet. It can be seen that: at 0.70 V, water velocity generally increases along the channel length and stabilizes close to the outlet; at 0.60 V water velocity is approximately uniform; and at 0.50 V, 0.40 V and 0.30 V water velocity tends to decrease along the channel. Such profiles generally agree with the local liquid water generation rate discussed above. The fluctuations of water velocity in the pores observed in Fig. 11 are due to differences in the area of the pores and the corresponding GDL bottom wall sections, used to compute water velocity. These deviations arise during mesh generation, and the subsequent discrete division of the GDL bottom wall into several zones.

4.4. Two-phase flow pressure drop

Pressure drop is an important parameter for the design of PEM fuel cell systems, especially when a compressor is used to supply air to the cathode side, as usually occurs in transportation applications. In such cases, higher pressure drops should be avoided because they lower the overall system efficiency. Pressure drop is also a reliable indicator of liquid water flooding, and water fault diagnosis approaches based on pressure drop have become popular [75]. The temporal evolution of two-phase flow pressure drop for different operating voltages is depicted in Fig. 12. First, it can be seen that pressure drop increases when the operating voltage decreases. This occurs because, as shown in Fig. 10, liquid water generation rate is higher for lower voltages, and higher water content in the channel raises the flow resistance. Second, an increase in pressure drop with respect to time is observed, due to water being continuously entering and accumulating in the channel. At some point, liquid water flow rate at the outlet is expected to match its emergence rate, and water content and consequently the two-phase flow pressure drop will stabilize.

4.5. Quantification of water content local distribution

As mentioned in the Introduction, one important issue of experimental techniques applied in the field of the two-phase flow in PEM fuel cells is the difficulty in getting precise quantitative information of water content location, although interesting progress has been achieved with image processing from optical visualization of liquid water inside transparent fuel cells [6,8,76]. Therefore, this section is dedicated to the quantification of water content in different locations of the serpentine channel. Such information complements the qualitative analysis of water dynamics presented in Section 4.2.

Fig. 13 shows the volume-weighted water content (volume of liquid water divided by the total volume) in the entire serpentine channel, in its straight sections and in its elbows, over time and for different operating voltages. For all cases, it can be seen that the volume-weighted water content in the elbows is considerably

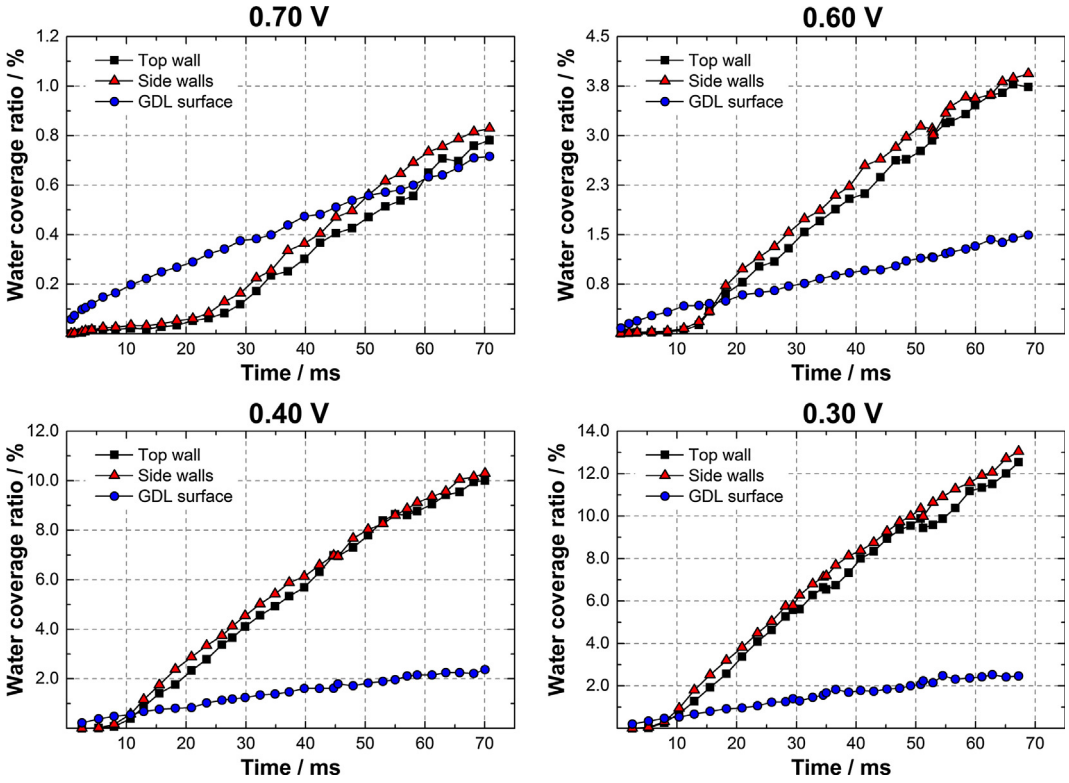

Fig. 15. Water coverage ratio at various operating voltages, at the top and side walls of the serpentine channel and at the GDL surface.

higher than that of the complete serpentine and its straight sections, except in the initial period when all droplets are still attached to the GDL surface (located in the straight sections). Such results were already expected taking into account the liquid water distribution in the GCs from Figs. 7 and 8. They also agree with that reported from direct visualization of liquid water distribution inside a transparent fuel cell with image processing [8]. It can also be observed that the relation of water content with the operating voltage as well as its temporal profile are in accordance with the results of the two-phase flow pressure drop, discussed in the section above.

The time-averaged volume-weighted water content in different sections of the serpentine channel is depicted in Fig. 14 for various voltages, after dividing the channel into 21 approximately equal sections, from the inlet to the outlet. The section 1 is that closest to the inlet and section 21 is that closest to the channel outlet. A graphical representation of the volume-weighted water content in each section over time would result into 21 lines for each voltage, and its interpretation would be very challenging. After a first analysis of the results, the authors verified that the trend of volume-weighted water content *vs* channel section remains generally constant over time. Therefore, the time-averaged volume-weighted water content for each channel is here shown for clarity. From the analysis of Fig. 14, it can be seen that the water content along the channel length generally agrees with the water velocity in each pore shown in Fig. 11, excepted for the case of the two first channel portions, which water content is lower than that of the following sections. This occurs because, contrarily to the other sections which are continuously being fed by water coming from upstream sections, section 1 does not have any section upstream and section 2 has just section 1.

Fig. 15 shows the water coverage ratio (area covered by liquid water divided by the total surface area) at the top and side walls of the serpentine channel, as well as at the GDL surface, over time and for various operating voltages. Except for 0.70 V, in which very little liquid water accumulates in the GC, it can be seen that the water coverage ratio of the top and side walls is considerably higher than that of the GDL surface. This is a desired scenario, because water accumulation in the GDL surface should be avoided, otherwise it would hamper the air flow through the GDL and the oxygen supply to the CL. The reason for higher water accumulation in the top and side walls is due to their hydrophilic nature that causes water to adhere to them, explaining the appearance of the water films visualized in Figs. 7 and 8. The results from Fig. 15

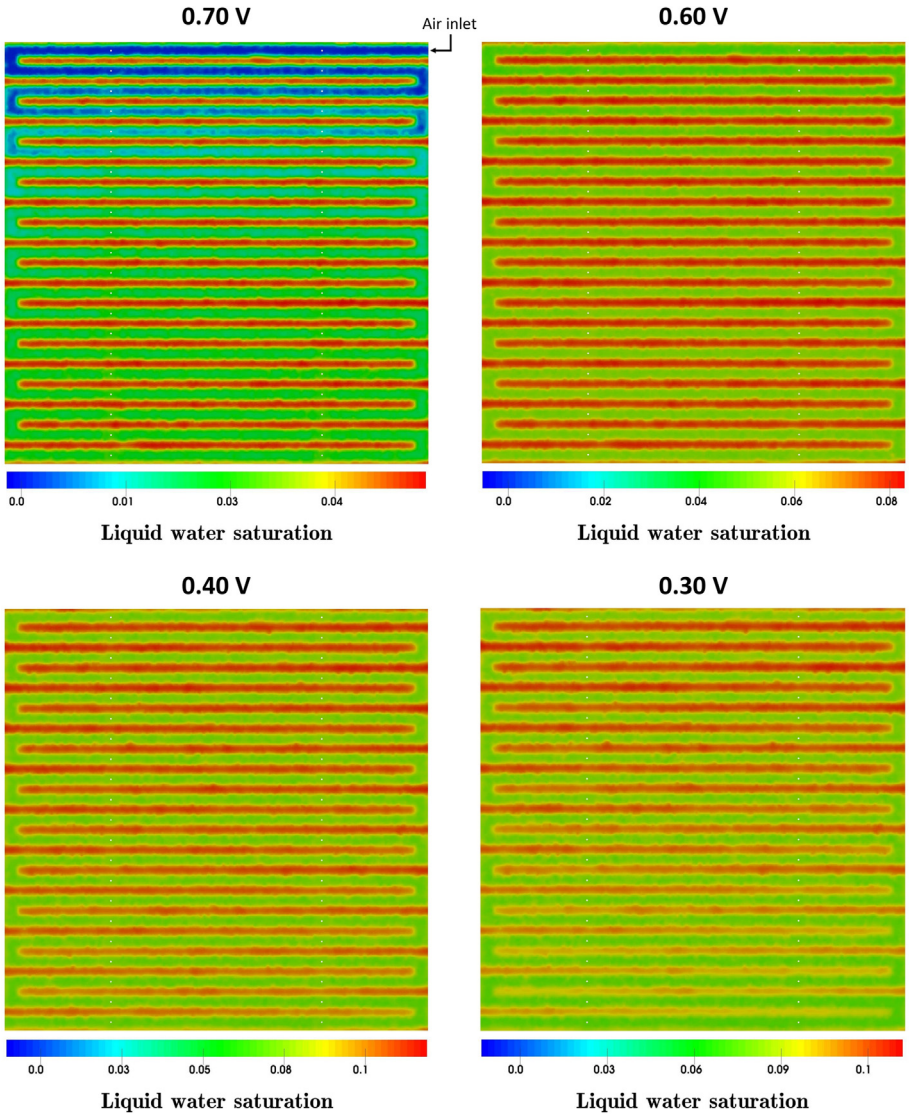

Fig. 16. Liquid water saturation distribution at the GDL bottom wall for various operating voltages.

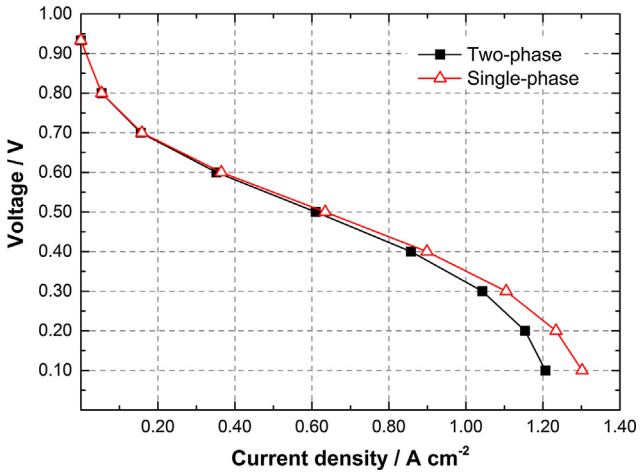

Fig. 17. Single-phase and two-phase flow predictions of the fuel cell performance in terms of polarization curve.

generally agree with those from other numerical studies that consider similar channel walls wettabilities and a hydrophobic GDL [26,77]. Moreover, they show that the approach adopted in the present model to account for the hydrophobicity of the GDL surface is valid.

4.6. Liquid water saturation and its effects on the cell performance

Fig. 16 shows liquid water saturation in the GDL bottom wall at various operating voltages. In general, liquid water saturation distribution along the channel length follows the same trend as liquid water generation rate, shown in Fig. 10 and discussed above. It can also be seen that more water is accumulated under the land region (the area not adjacent to the serpentine channel), because the convective flow is weaker than that in the region adjacent to the channel. Therefore, water is removed with greater difficulty from this location.

Fig. 17 contains single-phase and two-phase flow predictions of the cell performance in terms of polarization curve calculated by the present model. In single-phase flow calculations, liquid water saturation is set equal to 0 for all voltages, and in two-phase flow calculations the liquid water saturation shown in Fig. 16 (area-weighted average values) is used in Eqs. (14) and (37) to compute the effects of liquid water flooding: the decrease in the effective diffusion coefficient; and the coverage of the active sites of the CL, respectively. It can be seen that the present two-phase flow model estimates lower performances at high currents, where mass transfer limitations are dominant. Such results shown that the model can effectively account for the influence of flooding in the cell operation.

5. Conclusions

In this work, a 1D + 3D numerical model of a PEM fuel cell is described. It couples the VOF method to simulate the two-phase flow in the cathode GCs with the electrochemical reactions and the water balance in the membrane. Moreover, the multi-fluid saturation model is applied in order to obtain liquid water saturation in the GDL.

The model is successfully validated against an experimental polarization curve, and it can effectively separate the different voltage losses that affect the cell output. Moreover, visualization of liquid water distribution inside a transparent fuel cell is conducted, and it is shown that the model is capable of capturing some of the main two-phase flow patterns observed experimentally: water accumulation in the elbows of the serpentine channel and the formation of long water films attached to the side walls.

Water dynamics inside the serpentine channel for different voltages is analyzed. Water droplets emergence, detachment and interaction with the channel walls and other droplets are captured. At a lower voltage, droplets grow larger and suffer more deformation, and the amount of water accumulated in the channel is higher. Such fact is also noted when looking to the two-phase flow pressure drop, that increases when the voltage is decreased. It is also observed that, after a certain time, liquid water distribution in the channel does not change considerably over time.

Water velocity in each pore designed at the GDL surface for water emergence in the GCs is correlated with liquid water generation rate and current density distributions. It is found that, for a higher voltage, water velocity of the pores increases along the channel length, whereas at lower voltages it tends to decrease along the channel.

Water content in different locations of the serpentine is quantified and the results show that, as expected from the analysis of liquid water distribution, the volume-weighted water content is higher in the elbows of the serpentine channel. When dividing the serpentine into equal sections, from inlet to outlet, it is seen that water content along the channel length generally follows the same trend as the water velocity in the pores. It is also found that the water coverage ratio is significantly higher in the hydrophilic top and side walls of the channel in comparison with that at the GDL hydrophobic surface.

Single-phase and two-phase flow simulations are performed and it is observed that lower performances are predicted at high currents when the two-phase flow is considered, showing that the model can compute the effects of water flooding on the cell operation.

Acknowledgements

The doctoral fellowship SFRH/BD/89572/2012 of Rui B. Ferreira funded by the Portuguese "Fundação para a Ciência e Tecnologia" (FCT), POPH/QREN and European Social Fund (ESF) is acknowledged. D. S. Falcão and V. B. Oliveira thank the post-doctoral scholarships SFRH/BPD/109815/2015 and SFRH/BPD/91993/2012, respectively, also funded by FCT, POPH/QREN and ESF. POCI (FEDER) also supported this work via CEFT. This work was also supported by the european project PEMFC-SUDOE (SOE1/P1/E0293).

References

[1] Pei P, Chen H. Main factors affecting the lifetime of proton exchange membrane fuel cells in vehicle applications: A review. Appl Energy. 2014;125:60–75.
[2] Tüber K, Pócza D, Hebling C. Visualization of water buildup in the cathode of a transparent PEM fuel cell. J Power Sources 2003;124:403–14.
[3] Zhang F, Yang X, Wang C. Liquid water removal from a polymer electrolyte fuel cell. J Electrochem Soc 2006;153:A225–32.
[4] Ge S, Wang CY. Liquid water formation and transport in the PEFC anode. J Electrochem Soc 2007;154:B998–B1005.
[5] Hussaini IS, Wang CY. Visualization and quantification of cathode channel flooding in PEM fuel cells. J Power Sources 2009;187:444–51.
[6] Sergi JM, Kandlikar SG. Quantification and characterization of water coverage in PEMFC gas channels using simultaneous anode and cathode visualization and image processing. Int J Hydrogen Energy 2011;36:12381–92.
[7] Lee D, Bae J. Visualization of flooding in a single cell and stacks by using a newly-designed transparent PEMFC. Int J Hydrogen Energy 2012;37:422–35.
[8] Bozorgnezhad A, Shams M, Kanani H, Hasheminasab M, Ahmadi G. The experimental study of water management in the cathode channel of single-serpentine transparent proton exchange membrane fuel cell by direct visualization. Int J Hydrogen Energy 2015;40:2808–32.
[9] Jiao K, Park J, Li X. Experimental investigations on liquid water removal from the gas diffusion layer by reactant flow in a PEM fuel cell. Appl Energy 2010;87:2770–7.
[10] Feindel KW, LaRocque LPA, Starke D, Bergens SH, Wasylishen RE. In situ observations of water production and distribution in an operating H2/O2 PEM fuel cell assembly using 1H NMR microscopy. J Am Chem Soc 2004;126:11436–7.
[11] Dunbar Z, Masel RI. Quantitative MRI study of water distribution during operation of a PEM fuel cell using Teflon® flow fields. J Power Sources 2007;171:678–87.
[12] Satija R, Jacobson DL, Arif M, Werner S. In situ neutron imaging technique for evaluation of water management systems in operating PEM fuel cells. J Power Sources 2004;129:238–45.
[13] Pekula N, Heller K, Chuang PA, Turhan A, Mench MM, Brenizer JS, Ünlü K. Study of water distribution and transport in a polymer electrolyte fuel cell using neutron imaging. Nucl Instrum Meth A 2005;542:134–41.
[14] Kim T, Sim C, Kim M. Research on water discharge characteristics of PEM fuel cells by using neutron imaging technology at the NRF, HANARO. Appl Radiat Isot 2008;66:593–605.
[15] Iranzo A, Boillat P, Biesdorf J, Salva A. Investigation of the liquid water distributions in a 50 cm2 PEM fuel cell: Effects of reactants relative humidity, current density, and cathode stoichiometry. Energy 2015;82:914–21.
[16] Manke I, Hartnig C, Grünerbel M, Lehnert W, Kardjilov N, Haibel A, Hilger A, Banhart J, Riesemeier H. Investigation of water evolution and transport in fuel cells with high resolution synchrotron x-ray radiography. Appl Phys Lett 2007;90. 174105-1-3.
[17] Mukaide T, Mogi S, Yamamoto J, Morita A, Koji S, Takada K, Uesugi K, Kajiwara K, Noma T. In situ observation of water distribution and behaviour in a polymer electrolyte fuel cell by synchrotron X-ray imaging. J Synchrotron Radiat 2008;15:329–34.
[18] Antonacci P, Chevalier S, Lee J, Yip R, Ge N, Bazylak A. Feasibility of combining electrochemical impedance spectroscopy and synchrotron X-ray radiography for determining the influence of liquid water on polymer electrolyte membrane fuel cell performance. Int J Hydrogen Energy 2015;40:16494–502.
[19] Ferreira RB, Falcão DS, Oliveira VB, Pinto AMFR. Numerical simulations of two-phase flow in proton exchange membrane fuel cells using the volume of fluid method – A review. J Power Sources. 2015;277:329–42.
[20] Andersson M, Beale SB, Espinoza M, Wu Z, Lehnert W. A review of cell-scale multiphase flow modeling, including water management, in polymer electrolyte fuel cells. Appl Energy 2016;180:757–78.
[21] Le AD, Zhou B. A general model of proton exchange membrane fuel cell. J Power Sources 2008;182:197–222.
[22] Le AD, Zhou B. A generalized numerical model for liquid water in a proton exchange membrane fuel cell with interdigitated design. J Power Sources 2009;193:665–83.
[23] Le AD, Zhou B. Fundamental understanding of liquid water effects on the performance of a PEMFC with serpentine-parallel channels. Electrochim Acta 2009;54:2137–54.
[24] Le AD, Zhou B. A numerical investigation on multi-phase transport phenomena in a proton exchange membrane fuel cell stack. J Power Sources 2010;195:5278–91.
[25] Chen L, Cao T, Li Z, He Y, Tao W. Numerical investigation of liquid water distribution in the cathode side of proton exchange membrane fuel cell and its effects on cell performance. Int J Hydrogen Energy 2012;37:9155–70.
[26] Ding Y, Bi X, Wilkinson DP. 3D simulations of the impact of two-phase flow on PEM fuel cell performance. Chem Eng Sci 2013;100:445–55.
[27] Ding Y, Anderson R, Zhang L, Bi X, Wilkinson DP. Simulations of two-phase flow distribution in communicating parallel channels for a PEM fuel cell. Int J Multiphase Flow 2013;52:35–45.
[28] Ding Y, Bi XT, Wilkinson DP. Numerical investigation of the impact of two-phase flow maldistribution on PEM fuel cell performance. Int J Hydrogen Energy 2013;39:469–80.
[29] Vera M. A single-phase model for liquid-feed DMFCs with non-Tafel kinetics. J Power Sources 2007;171:763–77.
[30] Litster S, Sinton D, Djilali N. Ex situ visualization of liquid water transport in PEM fuel cell gas diffusion layers. J Power Sources 2006;154:95–105.
[31] Pasaogullari U, Wang CY. Two-phase modeling and flooding prediction of polymer electrolyte fuel cells. J Electrochem Soc 2005;152:A380–90.
[32] Mazumder S, Cole JV. Rigorous 3-D mathematical modeling of PEM fuel cells II. Model predictions with liquid water transport. J Electrochem Soc 2003;150: A1510–7.
[33] You L, Liu H. A two-phase flow and transport model for the cathode of PEM fuel cells. Int J Heat Mass Tran 2002;45:2277–87.
[34] Wang Z, Wang CY, Chen K. Two-phase flow and transport in the air cathode of proton exchange membrane fuel cells. J Power Sources 2001;94:40–50.
[35] Gurau V, Zawodzinski Jr TA, Mann Jr JA. Two-phase transport in PEM fuel cell cathodes. J Fuel Cell Sci Technol 2008;5:021009.
[36] He G, Ming P, Zhao Z, Abudula A, Xiao Y. A two-fluid model for two-phase flow in PEMFCs. J Power Sources 2007;163:864–73.
[37] Berning T, Djilali N. A 3D, multiphase, multicomponent model of the cathode and anode of a PEM fuel cell. J Electrochem Soc 2003;150:A1589–98.
[38] Quan P, Lai M. Numerical study of water management in the air flow channel of a PEM fuel cell cathode. J Power Sources 2007;164:222–37.
[39] Brackbill J, Kothe DB, Zemach C. A continuum method for modeling surface tension. J Comput Phys 1992;100:335–54.
[40] Quan P, Lai MC. Numerical simulation of two-phase water behavior in the cathode of an interdigitated proton exchange membrane fuel cell. J Fuel Cell Sci Technol 2010;7:011017.
[41] He G, Yamazaki Y, Abudula A. The effect of wall roughness on the liquid removal in micro-channels related to a proton exchange membrane fuel cell (PEMFC). J Power Sources 2010;195:1561–8.
[42] Barbir F. PEM fuel cells: theory and practice. second ed. Academic Press; 2013.
[43] Gostick JT, Fowler MW, Ioannidis MA, Pritzker MD, Volfkovich YM, Sakars A. Capillary pressure and hydrophilic porosity in gas diffusion layers for polymer electrolyte fuel cells. J Power Sources 2006;156:375–87.
[44] Fuller EN, Schettler PD, Giddings JC. New method for prediction of binary gas-phase diffusion coefficients. Ind Eng Chem 1966;58:18–27.
[45] Das PK, Li X, Liu Z-S. Effective transport coefficients in PEM fuel cell catalyst and gas diffusion layers: Beyond Bruggeman approximation. Appl Energy 2010;87:2785–96.
[46] Wang S, Wang Y. Investigation of the through-plane effective oxygen diffusivity in the porous media of PEM fuel cells: Effects of the pore size distribution and water saturation distribution. Int J Heat Mass Tran 2016;98:541–9.
[47] Wang Y, Wang S. Evaluation and modeling of PEM fuel cells with the Bruggeman correlation under various tortuosity factors. Int J Heat Mass Tran 2017;105:18–23.
[48] Leverett M. Capillary behavior in porous solids. Trans AIME 1941;142:152–69.
[49] Udell KS. Heat transfer in porous media considering phase change and capillarity—the heat pipe effect. Int J Heat Mass Tran 1985;28:485–95.
[50] Wang X, Wang Y, Chen Y, Si C, Su A, Lee DG. Proton exchange membrane fuel cell modeling with diffusion layer-based and sands-based capillary pressure correlations: Comparative study. J Taiwan Inst Chem Eng 2014;45:1532–41.
[51] Ramos-Alvarado B, Hernandez-Guerrero A, Ellis MW. Non-equilibrium two-phase model of the air-cathode of a PEM fuel cell based on GDL experimental water transport characteristics. J Power Sources 2013;232:376–88.
[52] Kumbur EC, Sharp KV, Mench MM. On the effectiveness of Leverett approach for describing the water transport in fuel cell diffusion media. J Power Sources 2007;168:356–68.
[53] Kumbur EC, Sharp KV, Mench MM. Validated leverett approach for multiphase flow in PEFC diffusion media: II. compression effect. J Electrochem Soc 2007;154:B1305–14.
[54] Kumbur EC, Sharp KV, Mench MM. Validated leverett approach for multiphase flow in PEFC diffusion media: I. Hydrophobicity Effect. J Electrochem Soc 2007;154:B1295–304.
[55] Kumbur EC, Sharp KV, Mench MM. Validated leverett approach for multiphase flow in PEFC diffusion media: III. Temperature effect and unified approach. J Electrochem Soc 2007;154:B1315–24.
[56] Ye Q, Nguyen TV. Three-dimensional simulation of liquid water distribution in a PEMFC with experimentally measured capillary functions. J Electrochem Soc 2007;154:B1242–51.
[57] Ding Y, Bi H, Wilkinson D. Three-dimensional numerical simulation of water droplet emerging from a gas diffusion layer surface in micro-channels. J Power Sources 2010;195:7278–88.
[58] Jiao K, Zhou B. Accelerated numerical test of liquid behavior across gas diffusion layer in proton exchange membrane fuel cell cathode. J Fuel Cell Sci Technol 2008;5:041011.
[59] Springer TE, Zawodzinski T, Gottesfeld S. Polymer electrolyte fuel cell model. J Electrochem Soc 1991;138:2334–42.
[60] O'Hayre R, Cha S, Colella W, Prinz FB. Fuel cell fundamentals. 1st ed. USA: John Wiley & Sons, Inc.; 2006.
[61] Youngs DL. Time-dependent multi-material flow with large fluid distortion. In: Morton KW, Baines MJ, editors. Numerical methods for fluid dynamics. New York: Academic Press; 1982. p. 273–85.
[62] Bazylak A, Sinton D, Djilali N. Dynamic water transport and droplet emergence in PEMFC gas diffusion layers. J Power Sources 2008;176:240–6.
[63] Ding Y, Bi H, Wilkinson DP. Three dimensional numerical simulation of gas–liquid two-phase flow patterns in a polymer–electrolyte membrane fuel cells gas flow channel. J Power Sources 2011;196:6284–92.

[64] Luo G, Ji Y, Wang C, Sinha PK. Modeling liquid water transport in gas diffusion layers by topologically equivalent pore network. Electrochim Acta 2010;55:5332–41.
[65] Sinha PK, Wang C. Pore-network modeling of liquid water transport in gas diffusion layer of a polymer electrolyte fuel cell. Electrochim Acta 2007;52:7936–45.
[66] Ferreira RB, Falcão DS, Oliveira VB, Pinto AMFR. Experimental study on the membrane electrode assembly of a proton exchange membrane fuel cell: effects of microporous layer, membrane thickness and gas diffusion layer hydrophobic treatment. Electrochim Acta 2017;224:337–45.
[67] Bednarek T, Tsotridis G. Issues associated with modelling of proton exchange membrane fuel cell by computational fluid dynamics. J Power Sources 2017;343:550–63.
[68] Nam JH, Kaviany M. Effective diffusivity and water-saturation distribution in single-and two-layer PEMFC diffusion medium. Int J Heat Mass Tran 2003;46:4595–611.
[69] DuPont. DuPont™ Nafion® PFSA Membranes - NR 211 and NR 212; 2009.
[70] Ashrafi M, Shams M, Bozorgnezhad A, Ahmadi G. Simulation and experimental validation of droplet dynamics in microchannels of PEM fuel cells. Heat Mass Transfer 2016;52:2671–86.
[71] Carton JG, Lawlor V, Olabi AG, Hochenauer C, Zauner G. Water droplet accumulation and motion in PEM (Proton Exchange Membrane) fuel cell mini-channels. Energy 2012;39:63–73.
[72] Le AD, Zhou B, Shiu H, Lee C, Chang W. Numerical simulation and experimental validation of liquid water behaviors in a proton exchange membrane fuel cell cathode with serpentine channels. J Power Sources 2010;195:7302–15.
[73] Yang X, Zhang F, Lubawy A, Wang C. Visualization of liquid water transport in a PEFC. Electrochem Solid-State Lett 2004;7:A408–11.
[74] Weng FB, Su A, Hsu CY, Lee CY. Study of water-flooding behaviour in cathode channel of a transparent proton-exchange membrane fuel cell. J Power Sources 2006;157:674–80.
[75] Pei P, Li Y, Xu H, Wu Z. A review on water fault diagnosis of PEMFC associated with the pressure drop. Appl Energy 2016;173:366–85.
[76] Bozorgnezhad A, Shams M, Kanani H, Hasheminasab M, Ahmadi G. Two-phase flow and droplet behavior in microchannels of PEM fuel cell. Int J Hydrogen Energy 2016;41:19164–81.
[77] Jo JH, Kim WT. Numerical simulation of water droplet dynamics in a right angle gas channel of a polymer electrolyte membrane fuel cell. Int J Hydrogen Energy 2015;40:8368–83.